Collective rotation from ab initio theory

CAPRIO, Mark A, MARIS, Pieter, VARY, James P and SMITH, Robin <http://orcid.org/0000-0002-9671-8599>

Published version

CAPRIO, Mark A, MARIS, Pieter, VARY, James P and SMITH, Robin (2015). Collective rotation from ab initio theory. International Journal of Modern Physics E, 24 (09), p. 1541002.

International Journal of Modern Physics E

Collective rotation from *ab initio* theory

M. A. Caprio
Department of Physics, University of Notre Dame, Notre Dame, Indiana 46556-5670, USA

P. Maris and J. P. Vary
Department of Physics and Astronomy, Iowa State University, Ames, Iowa 50011-3160, USA

R. Smith
School of Physics and Astronomy, University of Birmingham, Edgbaston, Birmingham, B15 2TT, UK

Through *ab initio* approaches in nuclear theory, we may now seek to quantitatively understand the wealth of nuclear collective phenomena starting from the underlying internucleon interactions. No-core configuration interaction (NCCI) calculations for p-shell nuclei give rise to rotational bands, as evidenced by rotational patterns for excitation energies, electromagnetic moments, and electromagnetic transitions. In this review, NCCI calculations of $^{7-9}$Be are used to illustrate and explore *ab initio* rotational structure, and the resulting predictions for rotational band properties are compared with experiment. We highlight the robustness of *ab initio* rotational predictions across different choices for the internucleon interaction.

Keywords: Nuclear rotation; no-core configuration interaction calculations; Be isotopes.

PACS numbers: 21.60.Cs, 21.10.-k, 21.10.Re, 27.20.+n

1. Introduction

The challenge of *ab initio* nuclear theory is to quantitatively predict the complex and highly-correlated behavior of the nuclear many-body system, starting from the underlying internucleon interactions. Significant progress has been made in the *ab initio* description of light nuclei through large-scale calculations.[1–7] We may now seek to understand the wealth of nuclear collective phenomena[8] through *ab initio* approaches.[5,9–12]

In particular, rotational bands emerge in *ab initio* no-core configuration interaction (NCCI)[6] calculations of p-shell nuclei.[13,14] Rotational patterns are found in the calculated level energies, electromagnetic moments, and electromagnetic transitions. Natural questions surrounding the emergence of rotation in *ab initio* calculations include:

(i) How recognizable is the rotation, from the calculated observables?
(ii) How robust is the prediction of rotation, both against limitations in the many-body calculation and, more fundamentally, against uncertainties in the internucleon interaction?
(iii) How, physically, does the rotation arise, or what is the intrinsic structure?
(iv) How well does the calculated rotation agree with experiment, when compared quantitatively?

However, to understand the emergence of rotation in NCCI calculations and address these questions, we must first consider the *ab initio* calculations themselves. NCCI calculations are, of necessity, carried out in a finite, truncated space. Computational restrictions limit the extent to which converged calculations can be obtained.

This review is based upon the ideas and results of recent analyses of rotation in *ab initio* NCCI calculations. A systematic study of the emergence of rotational bands in NCCI calculations of $^{7-12}$Be, using the JISP16 nucleon-nucleon interaction,[15] is presented in Refs. 13, 14, 16. The spin and orbital angular momentum structure of rotational states in ^{7}Li (the mirror nucleus to ^{7}Be) and ^{9}Be is investigated, using a chiral next-to-next-to-next-to-leading-order (N^{3}LO) interaction,[17] in Ref. 18. (NCCI calculations for the ground state rotational band in ^{12}C, although not considered in this review, are discussed in Refs. 19, 20, 21.) We highlight here the robustness of the *ab initio* rotational predictions across different choices for the internucleon interaction. In particular, in many of the illustrations, we compare the results of calculations based on two interactions obtained by very different procedures: the JISP16 interaction (mentioned above) and the chiral next-to-next-to-leading-order (NNLO) interaction NNLO$_{\rm opt}$.[22]

The approach of this review is not to attempt an exhaustive summary of the rotational phenomena noted in recent NCCI calculations, but rather to focus on exploring a few illustrative cases. Specifically, calculations of $^{7-9}$Be are used to illustrate emergent rotational phenomena and to exemplify some of the ideas involved in analysis of *ab initio* rotational structure. We begin by introducing the challenges in obtaining converged results for the relevant observables in *ab initio* calculations (Sec. 2). The definition of rotation in nuclei and its expected signatures are then briefly reviewed (Sec. 3). Successively richer examples of rotation in the Be isotopes are examined in Sec. 4: the even-even isotope ^{8}Be (Sec. 4.1), the odd-mass isotope ^{7}Be (Sec. 4.2), and rotational structure including excited bands (and both parities) in ^{9}Be (Sec. 4.3). Finally, we compare the rotational energy parameters extracted from *ab initio* calculations with those for the experimentally observed bands in $^{7-9}$Be (Sec. 5).

2. NCCI calculations and their convergence

In NCCI calculations, the nuclear many-body Schrödinger equation is formulated as a Hamiltonian matrix eigenproblem. The Hamiltonian is represented with respect to a basis of antisymmetrized products of single-particle states. Conventionally,

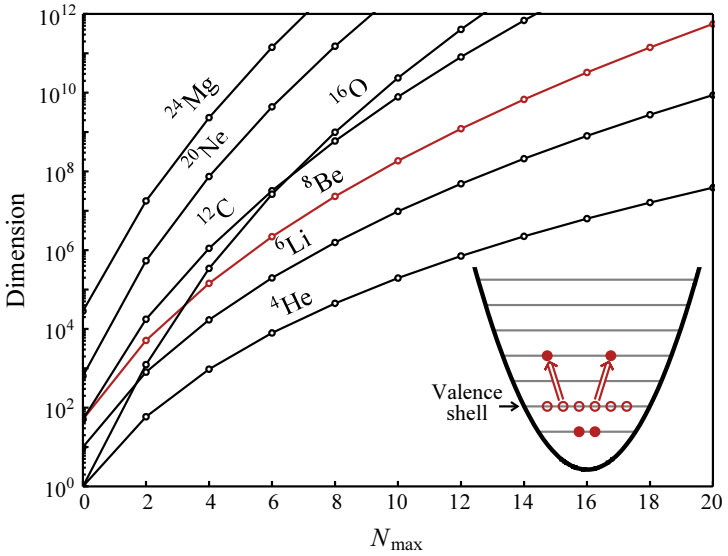

Fig. 1. Dimensions for NCCI calculations, as a function of the number of oscillator excitations $N_{\max}$ included in the basis, for selected nuclides. The example configuration shown (inset) involves a total of four oscillator excitations above the lowest oscillator configuration and thus would be included in calculations with $N_{\max} = 4$ and higher (for simplicity, only single particle states for one type of nucleon, protons or neutrons, are shown). Dimensions are shown for M-scheme natural parity, $M = 0$ spaces (see Sec. 4.1 text).

harmonic oscillator states[23] are used as the single-particle states, for the technical convenience they provide (both in transforming interaction matrix elements between relative and single-particle coordinates and in obtaining an exact separation of the center-of-mass wave function). The problem is then solved for the full system of A nucleons, *i.e.*, with no inert core.

In practice, calculations must be carried out in a finite-dimensional subspace, commonly obtained by truncating the basis to a maximum allowed number $N_{\max}$ of oscillator excitations. Convergence toward the exact results — as would be achieved in the full, infinite-dimensional space — is obtained with increasing $N_{\max}$. However, the basis size grows combinatorially with $N_{\max}$, so the maximum accessible $N_{\max}$ is severely limited by computational restrictions. The dimensions for representative cases are shown in Fig. 1 (and the meaning of $N_{\max}$ is illustrated in the inset). Thus, *e.g.*, $N_{\max} = 10$ calculations for ^{8}Be, as considered below, involve a Hamiltonian matrix dimension of $\sim 2 \times 10^{8}$.

The calculated eigenvalues and wave functions, and thus the calculated values for observables, depend both upon the basis truncation $N_{\max}$ and on the length parameter b for the oscillator basis functions, which is customarily specified by the equivalent oscillator energy $\hbar\omega$.[24] Any attempt to interpret the results of NCCI calculations (Sec. 4) or compare the calculations with experiment (Sec. 5) must

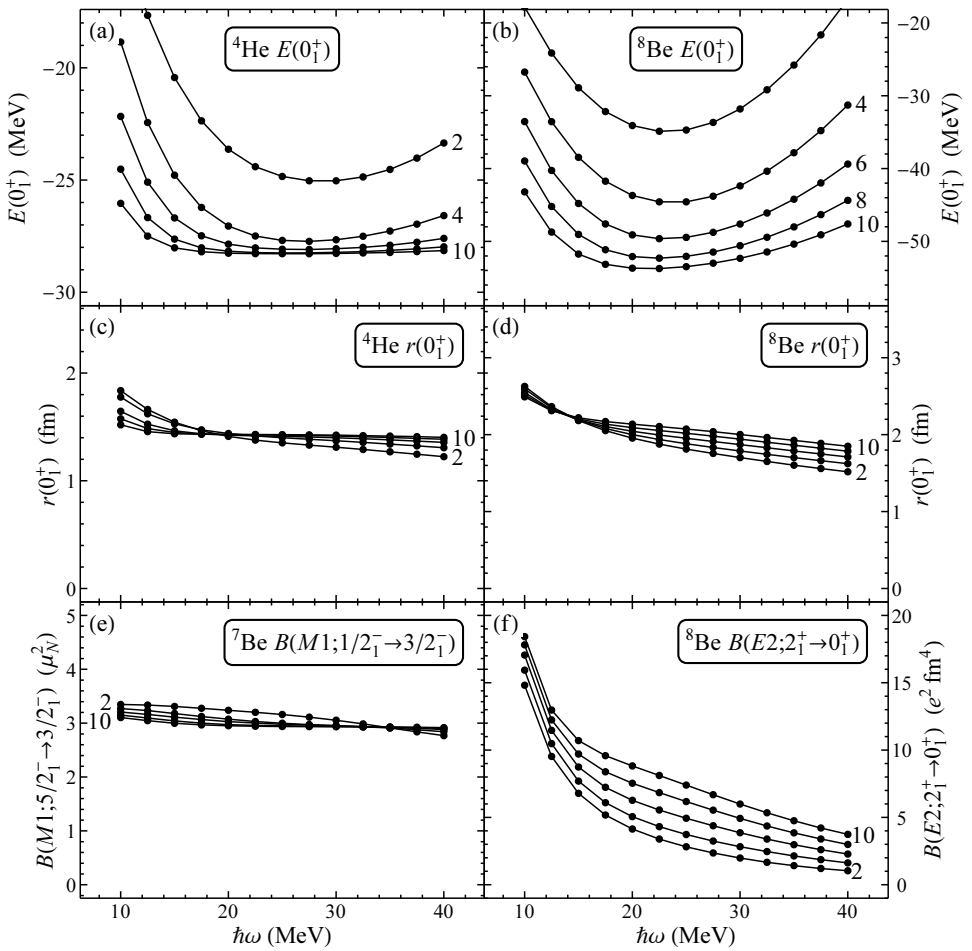

Fig. 2. The $N_{\max}$ and $\hbar\omega$ dependence of values obtained for observables in NCCI calculations, including comparatively converged and unconverged cases: (a) the ^{4}He ground state energy eigenvalue, (b) the ^{8}Be ground state energy eigenvalue, (c) the ^{4}He ground state RMS matter radius, (d) the ^{8}Be ground state RMS matter radius, (e) the magnetic dipole reduced transition probability between the first excited state and ground state of ^{7}Be, and (f) the electric quadrupole reduced transition probability between the first excited state and ground state of ^{8}Be. Calculated values are shown as functions of $\hbar\omega$ for $N_{\max} = 2$ to 10 (as labeled) and are obtained with the JISP16 nucleon-nucleon interaction, with Coulomb interaction between protons.

take into account the manner in which these observables approach convergence and the level of convergence which has been achieved.

The $N_{\max}$ and $\hbar\omega$ dependences of calculated ground-state energy eigenvalues are illustrated for ^{4}He in Fig. 2(a) and for ^{8}Be in Fig. 2(b), in both cases for $2 \leq N_{\max} \leq 10$ (we use the same $N_{\max}$ range in all calculations, for purposes of comparison, although current computational limits are significantly higher for ^{4}He). For a fixed $N_{\max}$, a minimum in the calculated energy is obtained at some $\hbar\omega$ (for the Be

isotopes this will typically be in the range $\hbar\omega \approx 20$–$25\,\mathrm{MeV}$). By the variational principle, any such calculated energy in a truncated space provides an upper bound on the true ground state energy in the full, untruncated many-body space. As $N_{\max}$ is increased, a lower calculated ground state energy is obtained at each $\hbar\omega$. The approach to convergence is marked by approximate $N_{\max}$ independence (a compression of successive energy curves) and $\hbar\omega$ independence (a flattening of each curve around its minimum). While a high level of convergence (at the keV scale) may be obtained in the lightest nuclei, in particular, for the tightly bound and compact nucleus ^{4}He [Fig. 2(a)], the situation is more challenging for the Be isotopes. The decrease in the variational minimum energy for ^{8}Be does become smaller with each step in $N_{\max}$ [Fig. 2(b)], but even at $N_{\max} = 10$ these changes are still at the MeV scale.

For electric quadrupole moments and transition strengths, traditionally so important in the identification of rotational structure,[25] convergence is even more elusive. The quadrupole operator, which has the form $Q_{2,m} \propto r^2 Y_{2,m}$,[24] includes an r^2 radial dependence and is therefore highly sensitive to the large-r "tails" of the nuclear wave function, which are poorly reproduced in a harmonic oscillator basis (see, *e.g.*, Fig. 1 of Ref. 26).

While it is difficult to come by an illustration of successful convergence of an electric quadrupole strength in NCCI calculations, the convergence of the root mean square (RMS) radius observable in ^{4}He, shown in Fig. 2(c), provides a model of the behavior which might be expected. The RMS radius, like quadrupole observables, is deduced from matrix elements of an operator with an r^2 dependence. Convergence — in general, manifested in $N_{\max}$ independence and $\hbar\omega$ independence — is here reflected in a compression of successive $N_{\max}$ curves and a flat "shoulder" in the plot of the $B(E2)$ against $\hbar\omega$, over some range of $\hbar\omega$ values. The calculated RMS radius of ^{8}Be, shown for comparison in Fig. 2(d), appears to be approaching convergence but is not fully converged.

Returning, finally, to the quadrupole observables, the calculated quadrupole transition strength between the 2^+ first excited state and 0^+ ground state of ^{8}Be is shown in Fig. 2(f). Here, the variation with $N_{\max}$ and $\hbar\omega$ is much greater,[a] and at most hints of the onset of convergence might be apparent. Consequently, there is no obvious way to extract quadrupole observables, at least in their absolute magnitudes. We shall see (Sec. 4) that relative values of different quadrupole observables within the same calculation may, nonetheless, be meaningfully considered.

[a]The greater $N_{\max}$ and $\hbar\omega$ dependence of the $B(E2)$ observable [Fig. 2(f)], as compared to the radius [Fig. 2(d)], is in part an artifact of the definition of the observable, rather than entirely reflecting a difference in the actual convergence properties of the underlying matrix element. The RMS radius is obtained by taking the *square root* of the expectation value [$\propto \langle r^2\rangle^{1/2}$], reducing any sensitivity to the matrix element, while the $B(E2)$ is obtained by taking the *square* of the matrix element [$\propto \langle r^2 Y_2\rangle^2$], amplifying any sensitivity to the matrix element. Roughly speaking, the total power difference of 4 in scaling with the radius between these two observables would be expected to quadruple all relative (percentage) sensitivities.

Magnetic dipole moments and transition strengths, in contrast, are comparatively well-converged. The $N_{\max}$ and $\hbar\omega$ dependence of the calculated dipole transition strength between the $1/2^-$ first excited state and $3/2^-$ ground state of ^{7}Be is shown in Fig. 2(e).

3. Collective nuclear rotation

To begin, we must define what is meant by rotation in the nuclear many-body system. Nuclear rotation[8,25] arises when there is an adiabatic separation of a rotational degree of freedom from the remaining internal degrees of freedom of the nucleus.

A rotational state factorizes into an *intrinsic state* $|\phi_K\rangle$ and a rotational wave function of the Euler angles ϑ, describing the collective rotational motion of this intrinsic state. Specifically, we consider an axially symmetric intrinsic state, with definite angular momentum projection K along the intrinsic symmetry axis. The full nuclear state $|\psi_{JKM}\rangle$, with total angular momentum J and projection M, has the form

$$|\psi_{JKM}\rangle \propto \int d\vartheta \, \big[\underbrace{\mathscr{D}^J_{MK}(\vartheta)}_{\text{Rotational}} \, \underbrace{|\phi_K;\vartheta\rangle}_{\text{Intrinsic}} \; + \; (-)^{J+K} \mathscr{D}^J_{M,-K}(\vartheta) |\phi_{\bar{K}};\vartheta\rangle \big], \tag{1}$$

where $|\phi_K;\vartheta\rangle$ represents the intrinsic state $|\phi_K\rangle$ after rotation by ϑ, and the wave function $\mathscr{D}^J_{MK}(\vartheta)$ in the Euler angles is a Wigner $\mathscr{D}$ function. The second term, involving the $\mathscr{R}_2$-conjugate state $|\phi_{\bar{K}};\vartheta\rangle$, arises from discrete rotational symmetry considerations, *i.e.*, under an "end-over-end" rotation $\mathscr{R}_2$ by an angle π about an axis perpendicular to the symmetry axis.

The recognizable signatures of rotational structure reside not in the observables for the states considered singly, but in relationships among different rotational states arising from their closely-related wave functions (1). A *rotational band* is comprised of nuclear states sharing the same intrinsic state $|\phi_K\rangle$ but differing in the angular momentum J of their rotational motion, *i.e.*, differing in their angular wave functions $\mathscr{D}^J_{MK}(\vartheta)$. Within a rotational band, $J = K, K+1, \ldots$, except for $K = 0$ bands, where only even J or only odd J are present (depending upon the $\mathscr{R}_2$ symmetry). Energies and electromagnetic multipole matrix elements among band members follow well-defined rotational patterns.

Band members are expected to have energies following the rotational formula $E(J) = E_0 + AJ(J+1)$, where the rotational energy constant $A \equiv \hbar^2/(2\mathcal{J})$ is inversely related to the moment of inertia $\mathcal{J}$ of the intrinsic state. For $K = 1/2$ bands, the Coriolis contribution to the kinetic energy significantly modifies this pattern, yielding an energy staggering

$$E(J) = E_0 + A\big[J(J+1) + \underbrace{a(-)^{J+1/2}(J+\tfrac{1}{2})}_{\text{Coriolis } (K=1/2)}\big], \tag{2}$$

where a is the Coriolis decoupling parameter.

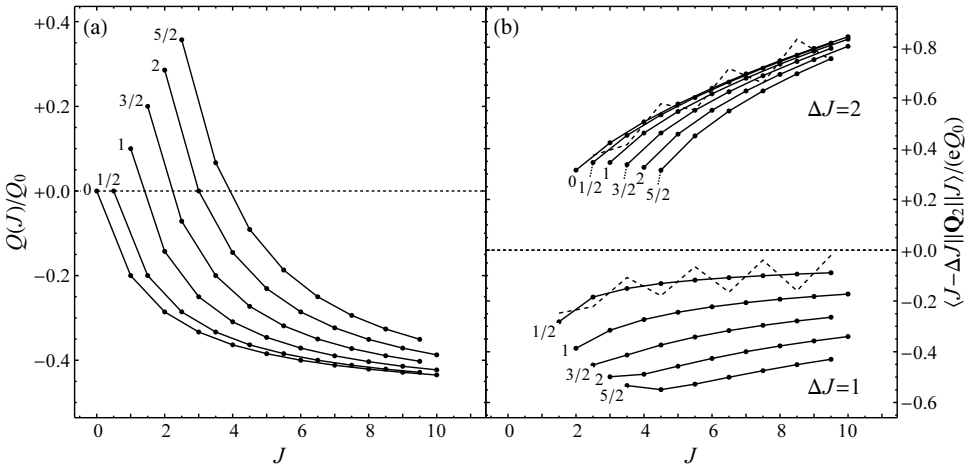

Fig. 3. Rotational predictions for electric quadrupole (a) moments and (b) transition reduced matrix elements, within a rotational band, normalized to the intrinsic quadrupole moment Q_0, shown for bands with $0 \leq K \leq 5/2$, as indicated. The further possibility of staggering of transition strengths within a $K = 1/2$ band[14] is indicated by the dotted lines. Figure from Ref. 14.

For the electric quadrupole operator, in particular, the reduced matrix element between band members (with initial and final angular momenta J_i and J_f, respectively) follows the relation[b]

$$\langle \Psi_{J_f K} \| \mathbf{Q}_2 \| \Psi_{J_i K} \rangle = (2J_i + 1)^{1/2} \underbrace{(J_i K 20 | J_f K)}_{\text{Rotational}} \underbrace{\langle \phi_K | Q_{2,0} | \phi_K \rangle}_{\text{Intrinsic } (\propto eQ_0)} . \tag{3}$$

The value depends on the particular band members involved, J_i and J_f, only through the Clebsch-Gordan coefficient, while the specific structure of the intrinsic state enters only through the intrinsic quadrupole moment $eQ_0 \equiv (16\pi/5)^{1/2} \langle \phi_K | Q_{2,0} | \phi_K \rangle$.

All electric quadrupole moments $Q(J)$ and reduced transition probabilities $B(E2; J_i \to J_f)$ within a given band are therefore uniquely related to each other via (3), simply from the assumption of rotation, with their overall normalization determined by Q_0. That is,

$$Q(J) = \frac{3K^2 - J(J+1)}{(J+1)(2J+3)} Q_0, \tag{4}$$

and

$$B(E2; J_i \to J_f) = \frac{5}{16\pi} (J_i K 20 | J_f K)^2 (eQ_0)^2. \tag{5}$$

[b]Notations for electromagnetic observables and the convention for reduced matrix elements are as defined in Sec. II of Ref. 14. Also see this reference for discussion of a cross term omitted from (3), which may arise for bands with $K = 1/2$ or 1.

Experimental transition strengths are customarily expressed in terms of the *unsigned* reduced transition probabilities — or $B(E2)$ values — as given in (5), since phase information on the matrix elements is not normally experimentally accessible. However, in the rotational analysis of *ab initio* wave functions it is more informative to consider the *signed* (unsquared) reduced matrix elements (3) directly, to retain further meaningful phase information (as illustrated in Sec. 4.2). The expected rotational relations for electric quadrupole moments and transition reduced matrix elements are summarized graphically in Fig. 3, for different values of K.

The rotational relation (3) is equally valid whether we take the quadrupole operator to be the proton quadrupole tensor (*i.e.*, the physical electric quadrupole operator) $\mathbf{Q}_p$ or the neutron quadrupole tensor $\mathbf{Q}_n$. The matrix elements of these two operators provide valuable complementary information for investigating rotation in *ab initio* calculations — despite the comparative (though not complete[27]) inaccessability of neutron quadrupole observables in traditional experimental analyses.

Magnetic dipole moments and transitions are deduced from reduced matrix elements of the magnetic dipole operator. The rotational predictions are based on the assumption of separation of the nucleus into a deformed rotational core, which contributes through an effective dipole operator simply proportional to $\mathbf{J}$, plus extra-core nucleons, which contribute through a residual magnetic dipole operator $\mathbf{M}'$. The result is a somewhat more complicated rotational expression

$$\begin{aligned}\langle \psi_{J_f K} \| \mathbf{M}_1 \| \psi_{J_i K} \rangle = \sqrt{\tfrac{3}{4\pi}} g_R \mu_N \langle J_f \| \mathbf{J} \| J_i \rangle \delta_{J_i J_f} \\ + (2J_i+1)^{1/2} \Big[(J_i K 10 | J_f K) \langle \phi_K | M'_{1,0} | \phi_K \rangle \\ + \delta_{K,1/2} (-)^{J_i + 1/2} (J_i, -\tfrac{1}{2}, 1, 1 | J_f \tfrac{1}{2}) \langle \phi_{1/2} | M'_{1,1} | \phi_{\overline{1/2}} \rangle \Big],\end{aligned} \tag{6}$$

for which corresponding simplified expressions for dipole moments $\mu(J)$ or $\Delta J = 1$ transitions may be found in Sec. II D of Ref. 14. The essential point for purposes of rotational analysis is to note that the rotational predictions involve three parameters: a core rotational gyromagnetic ratio g_R (affecting only moments), a direct intrinsic matrix element $\langle \phi_K | M'_{1,0} | \phi_K \rangle$, and a cross term intrinsic matrix element $\langle \phi_{1/2} | M'_{1,1} | \phi_{\overline{1/2}} \rangle$ (for $K = 1/2$ bands). The contributions to the magnetic dipole matrix elements from these various terms are summarized graphically in Fig. 4, for different values of K.

The physical magnetic dipole operator (excluding meson-exchange currents) is the particular linear combination of orbital/spin and proton/neutron angular momentum operators

$$\mathbf{M}_1 = \sqrt{\frac{3}{4\pi}} \mu_N \big(g_{\ell,p} \mathbf{L}_p + g_{\ell,n} \mathbf{L}_n + g_{s,p} \mathbf{S}_p + g_{s,n} \mathbf{S}_n \big), \tag{7}$$

where the physical gyromagnetic ratios are $g_{\ell,p} = 1$, $g_{\ell,n} = 0$, $g_{s,p} \approx 5.586$, and $g_{s,n} \approx -3.826$. However, the rotational results (6) apply to each term independently (and to any such linear combination). Therefore, magnetic dipole matrix elements

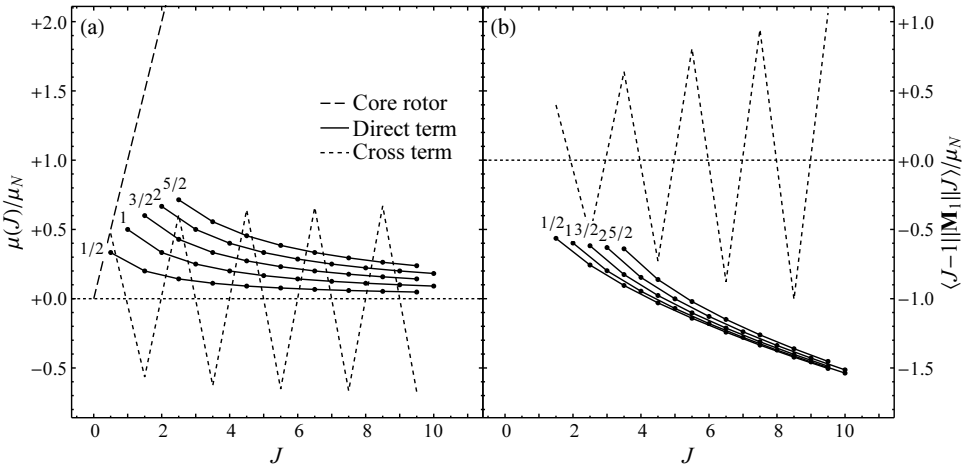

Fig. 4. Rotational predictions for each of the terms in (6) contributing to magnetic dipole (a) moments and (b) transition reduced matrix elements, within a rotational band: the core rotor term for dipole moments (dashed line), direct term (solid lines, $K \geq 1/2$ only, as indicated), and cross term (dotted lines, $K = 1/2$ only). For purposes of comparison, the curves are shown with normalizations given by $g_R = 1$ and intrinsic matrix elements equal to $[3/(4\pi)]^{1/2}\mu_N$. Figure from Ref. 14.

may be calculated and analyzed considering each of these different *dipole terms*[24] individually, to separately probe the orbital and spin angular momentum structure of rotation.[c] The magnetic dipole moment or magnetic dipole transition matrix element pertinent to physical electromagnetic transitions can, of course, be recovered as the particular linear combination given in (7).

4. Emergence of rotational bands in the Be isotopes

4.1. *Rotation in* ^{8}Be

Let us begin with the simplest case, that of the even-even nucleus ^{8}Be. The level energies obtained in *ab initio* NCCI calculations of ^{8}Be are shown in Fig. 5.

Traditionally, two competing structural descriptions may be invoked.[28] In a cluster description, this nucleus consists of two α particles, which may undergo rotation analogous to that of a diatomic molecule, resulting in a $K = 0$ positive parity yrast rotational band (with $J = 0, 2, 4, \ldots$). However, in a conventional shell-model description, limited to the p-shell valence space, only states with angular momentum $J \leq 4$ can be constructed.

[c]Specifically, the magnetic dipole observables quoted for each of these operators will be obtained by setting the corresponding gyromagnetic ratio to unity, *i.e.*, using $M1$ operators defined for each dipole term as $\mathbf{D}_{\ell,p} = [3/(4\pi)]^{1/2}\mu_N\mathbf{L}_p$, $\mathbf{D}_{\ell,n} = [3/(4\pi)]^{1/2}\mu_N\mathbf{L}_n$, *etc.*[14] Of course, if one were willing to move further away from traditional notation for magnetic dipole observables, one could just as well quote matrix elements of $\mathbf{L}_p$, $\mathbf{L}_n$, *etc.*, directly.

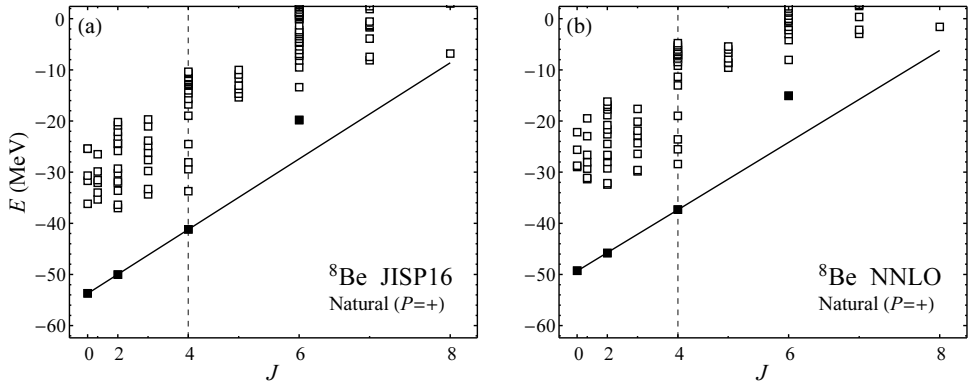

Fig. 5. Energy eigenvalues for states in the natural parity space of ^{8}Be, as obtained with the JISP16 (left) and NNLO (right) nucleon-nucleon interactions. Energies are plotted with respect to an angular momentum axis which is scaled to be linear in $J(J+1)$. Solid symbols indicate candidate band members. Lines indicate the corresponding fits for rotational energies (2). Vertical dashed lines indicate the maximal angular momentum accessible within the lowest harmonic oscillator configuration (or valence space). From calculations with $N_{\max} = 10$ at $\hbar\omega = 20\,\mathrm{MeV}$.

Experimentally, ^{8}Be is unbound, but the "ground state" consists of a narrow $J = 0$ resonance, which decays by 2α breakup.[29] The next excited levels are $J = 2$ and 4 resonances. The energies are approximately consistent with a rotational pattern, with the experimental $E(4^+)/E(2^+) \approx 3.75(5)$ lying somewhat above the expected rotational value of $10/3 \approx 3.33$. Since the 2α decay mode so completely dominates over electromagnetic decay, ratios of electromagnetic transition matrix elements among these states are not known experimentally (only the $4^+ \to 2^+$ transition has been observed[30]).

Before further interpreting the results in Fig. 5, a few comments are in order defining the specifics of the calculations (applicable also to the calculations discussed in subsequent sections for ^{7,9}Be). The calculations are obtained using two different realistic nucleon-nucleon interactions. The JISP16 interaction[15] [Fig. 5(a)] is a charge-independent two-body interaction derived from nucleon-nucleon scattering data and adjusted via a phase-shift equivalent transformation to describe light nuclei without explicit three-body interactions.[d] The $\mathrm{NNLO_{opt}}$ interaction[22] [Fig. 5(b)] is obtained from chiral effective field theory at next-to-next-to-leading order (NNLO), with low-energy constants chosen to reproduce nucleon-nucleon scattering phase shifts.

The many-body Hamiltonian eigenproblem is then solved using the code

[d]The present calculations also include the Coulomb interaction between protons. It should be noted that these calculations are therefore not identical to the JISP16 calculations previously presented in Refs. 13, 14, 16, in which the Coulomb interaction was omitted, to ensure exact conservation of isospin. However, the primary effect of the Coulomb interaction is simply to induce a shift in the overall binding energies, which is irrelevant to the analysis of rotational band observables.

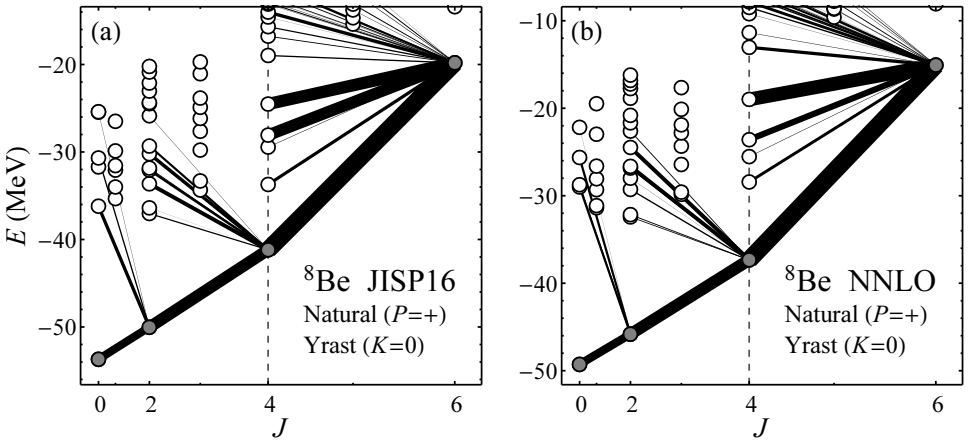

Fig. 6. Electric quadrupole transition strengths among levels in the ^{8}Be natural parity space, orignating from yrast band members, as obtained with the JISP16 (left) and NNLO (right) nucleon-nucleon interactions. Shaded symbols indicate the initial levels being considered. All angular momentum *decreasing* transitions from the selected levels are shown. Line thicknesses are proportional to the magnitude of the reduced matrix element for the transition (also conveyed through a gray scale). From calculations with $N_{\max} = 10$ at $\hbar\omega = 20\,\mathrm{MeV}$, using the proton quadrupole tensor.

MFDn,[31–33] in a proton-neutron M scheme basis.[34] States of different parity are solved for separately. The states shown in Fig. 5 are in the natural parity space.[e] The calculations in Fig. 5 are obtained for a specific choice of basis length parameter ($\hbar\omega = 20\,\mathrm{MeV}$) and trunction ($N_{\max} = 10$). They thus may be thought of as taking a "snapshot" of the spectrum along the path to convergence.

Energies following a rotational pattern are most easily recognized if plotted against an angular momentum axis which is scaled as $J(J+1)$, as in Fig. 5, so that energies in an ideal rotational band lie on a straight line (or staggered about a straight line, for $K = 1/2$). Rotational bands are most readily identifiable near the yrast line, where the density of states remains comparatively low. The band members are identified — both in the present discussion of ^{8}Be and in the subsequent discussions of other isotopes — on the basis not only of their energies, but also on the basis of collective enhancement of electric quadrupole transition strengths among band members. The strengths of the various electric quadrupole transitions originating from the candidate band members in ^{8}Be are shown in Fig. 6.

[e]The parity of the lowest allowed oscillator configuration, or traditional shell model valence space, may be termed the *natural parity*, and states of natural parity are more generally built from oscillator configurations with even numbers of excitations. The parity obtained by promoting one nucleon by one shell may be termed the *unnatural parity*, and states of unnatural parity are built from oscillator configurations with odd numbers of excitations. Thus, for even-mass p-shell nuclei, such as ^{8}Be, natural parity is positive parity, while, for odd-mass p-shell nuclei, such as ^{7,9}Be, natural parity is negative parity.

The candidate yrast rotational band members for ^{8}Be are indicated (solid symbols) in Fig. 5, through $J = 6$. Qualitatively, the situation is similar in the calculations with either the JISP16 interaction [Fig. 5(a)] or NNLO interaction [Fig. 5(b)]. The yrast $J = 0$, 2, and 4 states are well-isolated in energy from the off-yrast states and lie approximately on a straight line plotted with respect to $J(J + 1)$ (the line shown in Fig. 5 is the best rotational energy fit to the calculated band members, specifically, with $J \leq 4$). Their energies approximately match the rotational expectation, with $E(4^+)/E(2^+) \approx 3.42$ or 3.46, respectively, for the two calculations shown. While the energy of the calculated yrast $J = 6$ state lies well above the rotational line (Fig. 5), the quadrupole transition strengths (Fig. 6) nonetheless suggest that this state is a member of the yrast band: it is connected to the yrast 4^+ band member with collective strength, as well as, less strongly, to other off-yrast 4^+ states. Candidate 8^+ band members may be identified, as well, but they lie off the yrast line (and outside the energy range shown in Fig. 5).

Let us return to the challenge of convergence (Sec. 2), but now with rotational energy patterns in mind. The underlying question is how, when the calculated energies are still shifting on an MeV scale with increasing basis size, rotational patterns can nonetheless be reproduced at an MeV or sub-MeV scale. The $N_{\max}$ dependence of the energy eigenvalues is shown for the members of the yrast band in Fig. 7 (top). For each step in $N_{\max}$, the calculated energies shift lower by several MeV, much as already seen for the ground state energy in Fig. 2(b). However, it may also be noticed that the energies of different band members move downward in approximate synchrony as $N_{\max}$ increases (at least for the $J = 0$, 2, and 4 band members). Thus, the *relative* energies *within* the band remain comparatively unchanged, as is seen more directly when we consider excitation energies, in Fig. 7 (bottom). Thus, a rotational pattern in the relative energies remains robustly present, even as the energy eigenvalues themselves change. Moreover, the slope or, equivalently, rotational constant A would seem to be essentially converged.

There is, however, a clear difference in the convergence properties of the $J = 6$ band member, which lies above the maximal angular momentum ($J = 4$) accessible within the valence space or, equivalently, maximal angular momentum accessible within $N_{\max} = 0$ NCCI calculations (dashed vertical lines in Fig. 7). While the energy of the $J = 6$ band member lies above the rotational expectation, this energy is also converging downward relative to the energies of the lower band members.

Moving now to electromagnetic observables, recall that the calculated electric quadrupole matrix elements for ^{8}Be are far from converged, as we have seen in particular for the transition between the $J = 2$ and $J = 0$ band members [Fig. 2(f)]. However, rotational structure is reflected not in the values of these observables on an *absolute* scale, but rather on the *ratios* of matrix elements within a band, as dictated by the Clebsch-Gordan factor in the rotational formula (3). (The overall normalization of these matrix elements is then determined by the intrinsic structure, via the intrinsic quadrupole moment Q_0.) Let us therefore consider the *relative*

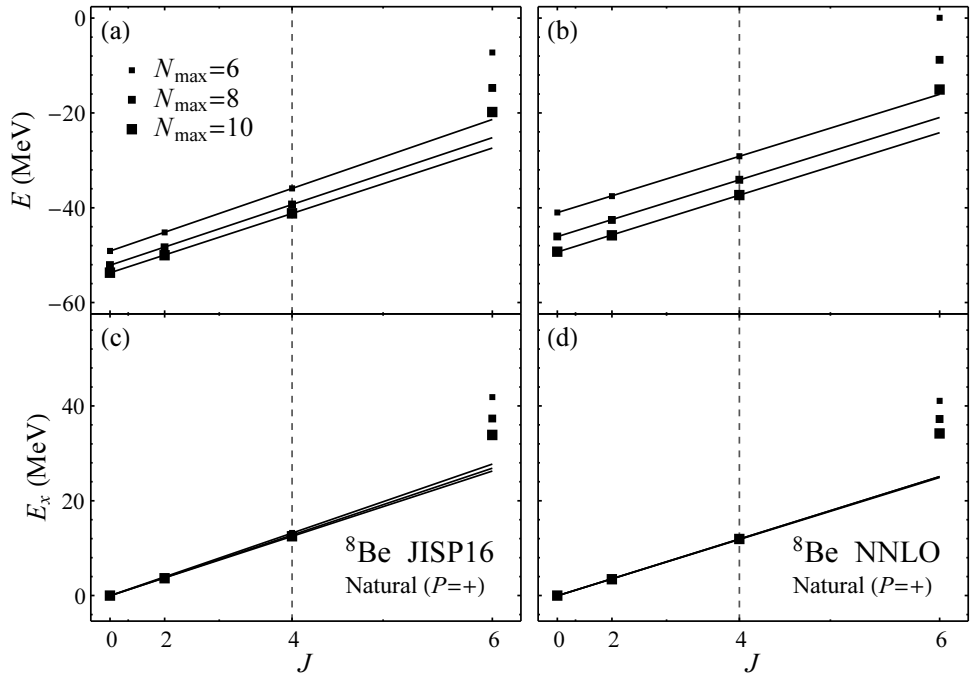

Fig. 7. Dependence of calculated energies for ^{8}Be natural parity yrast band members on $N_{\max}$: energy eigenvalues E (top) and excitation energies E_x (bottom), as obtained with the JISP16 (left) and NNLO (right) nucleon-nucleon interactions. Larger symbols indicate higher $N_{\max}$ values. Lines indicate the corresponding fits for rotational energies (2). Vertical dashed lines indicate the maximal valence angular momentum. From calculations with $N_{\max} = 6$, 8, and 10 at $\hbar\omega = 20$ MeV.

values of the quadrupole moments (proportional to diagonal matrix elements of the quadrupole operator) within the yrast band of ^{8}Be, in Fig. 8 (top) and, similarly, the quadrupole transition reduced matrix elements (or off-diagonal matrix elements of the quadrupole operator), in Fig. 8 (middle). The overall normalization Q_0 is eliminated by normalizing to one of these values. We choose to normalize to the first nonvanishing quadrupole moment within the band, *i.e.*, of the $J = 2$ band member. That is, the value of Q_0 used for normalization in Fig. 8 is determined from the calculated $Q(2)$ via (4). Results are shown both for the JISP16 interaction (at left) and the NNLO interaction (at right). In each case, the *relative* quadrupole matrix elements within the band are seen to be largely converged with respect to $N_{\max}$.

The expected rotational values for the quadrupole moments and transition matrix elements, from (3) and (4), are given by the curves in Fig. 8 (top, middle). Notice, comparing the left and right columns of Fig. 8, that the calculated quadrupole observables obtained with the JISP16 and NNLO interactions are virtually identical, not only in their resemblance to rotational predictions but also in the nature of their deviations from the rotational predictions. It should be emphasized that the

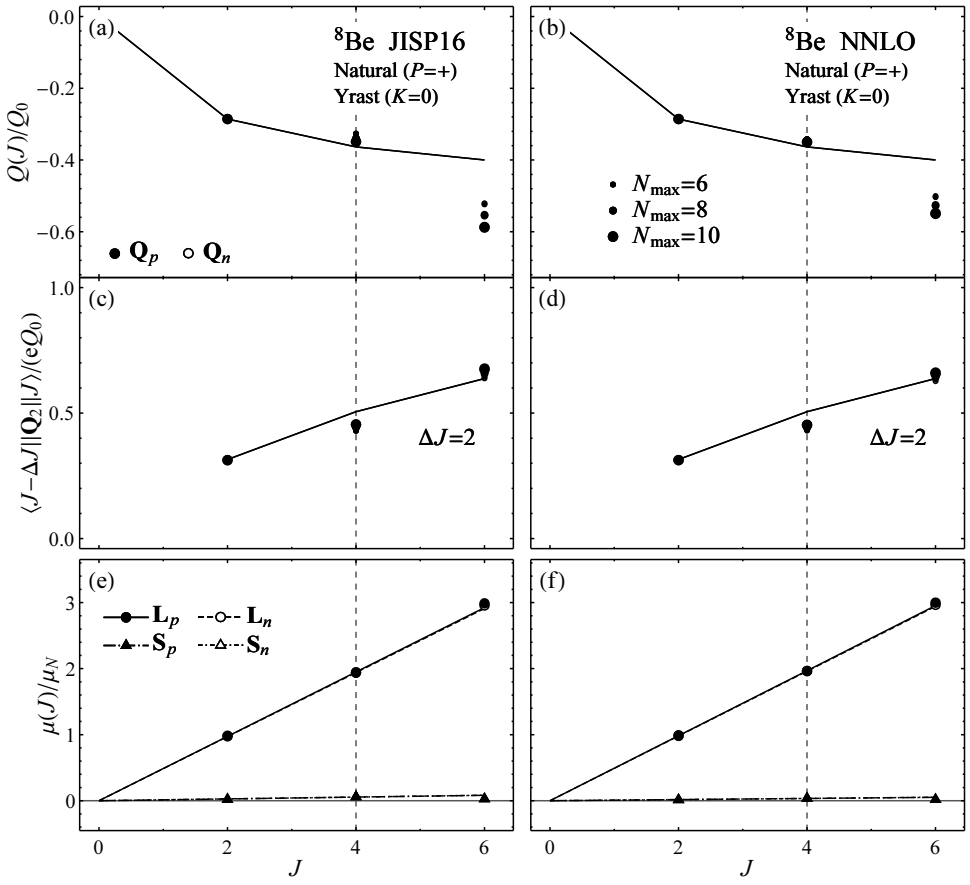

Fig. 8. Quadrupole and dipole matrix element observables for the ^{8}Be natural parity yrast band and their dependence on the $N_{\max}$ truncation: quadrupole moments (top), quadrupole transition reduced matrix elements (middle), and dipole moments (bottom), as obtained with the JISP16 (left) and NNLO (right) nucleon-nucleon interactions. Larger symbols indicate higher $N_{\max}$ values. Quadrupole observables are normalized to Q_0 (see text). Quadrupole observables calculated using both proton and neutron operators and dipole observables calculated using all four dipole terms are shown (but proton and neutron values nearly coincide in all cases). The curves indicate rotational values (for dipole observables, based on a best fit at highest $N_{\max}$). The vertical dashed lines indicate the maximal valence angular momentum. From calculations with $N_{\max} = 6$, 8, and 10 at $\hbar\omega = 20\,\mathrm{MeV}$.

same Q_0 values are used for normalization of the transitions [Fig. 8(c) or (d)] as for the quadrupole moments in the same calculation [Fig. 8(a) or (b), respectively]. Therefore, no free normalization parameter remains for the transition matrix elements. For example, since the value of Q_0 used for normalization in Fig. 8 is determined from $Q(2)$, the proximity of the lowest calculated transition data point to the rotational curve indicates that the *ab initio* calculations exhibit an agreement between $Q(2)$ and $B(E2; 2^+ \to 0^+)$ consistent with adiabatic rotation. There is a

break from the rotational predictions in the quadrupole moments at $J = 6$ — the quadrupole moment $Q(6)$ has the expected sign but is nearly half again as large in magnitude as expected from the rotational formula (and still increasing in magnitude with increasing $N_{\max}$). On the other hand, the transition matrix element from this $J = 6$ band member is still reasonably consistent with the rotational formula.

Since the difference between proton and neutron quadrupole observables will take on more significance going forward to the other Be isotopes (Secs. 4.2–4.3), it is worth noting that, for ^{8}Be, the matrix elements calculated using the proton and neutron quadrupole operators — $\mathbf{Q}_p$ and $\mathbf{Q}_n$ (Sec. 3) — are almost identical, as a result of the approximate proton-neutron symmetry of the system. Quadrupole moments and matrix elements calculated using the proton (solid symbols) and neutron (open symbols) quadrupole tensors are, in principle, both shown in Fig. 8, but the data points are almost entirely indistinguishable on the plot. The proton and neutron quadrupole observables are normalized separately in Fig. 8, *i.e.*, the proton and neutron intrinsic quadrupole moments ($Q_{0,p}$ and $Q_{0,n}$, respectively) are determined independently. Most of the difference in the calculated proton and neutron observables is embodied in this normalization, through an $\sim 1\%$ difference in $Q_{0,p}$ and $Q_{0,n}$.

There are no magnetic dipole transitions to consider within a $K = 0$ band, since the angular momenta of successive band members differ by 2. However, we may still examine the dipole moments for the rotational band members in ^{8}Be, as shown in Fig. 8 (bottom). As a particular special case of (6), these are expected to vary linearly with J, as $\mu(J) = g_R \mu_N J$. The dipole moments calculated with the orbital angular momentum dipole terms [circles in Fig. 8 (bottom)] do indeed closely follow such a linear relation. The values are well-converged, with a slope $g_R \approx 0.49$.[f] Note that the calculated dipole moments agree with the simple linear rotational formula even for the $J = 6$ band member, for which the calculated energy and quadrupole moment were not as clearly consistent with a rotational picture.

For the spin dipole terms [triangles in Fig. 8 (bottom)], the moments are nearly vanishing. The dipole moments calculated with the different orbital/spin and proton/neutron dipole terms may be interpreted as "spin contributions" coming from these different operators,[36] since they measure the projection of the orbital or spin angular momentum onto the total angular momentum. The near-vanishing contribution from the intrinsic spins is consistent with an α-clustering picture, where the spins pair to zero angular momentum.

Returning to the complementary shell model description, it may be noted that Elliot SU(3) symmetry[37,38] and the LS coupling scheme play significant organizing roles in the structure of p-shell nuclei.[39] *Ab initio* calculations of the ^{8}Be ground state in an SU(3) coupling scheme have been reported in Ref. 12, using a next-

[f]The traditional collective result for the gyromagnetic ratio[35] is $g_R = 0.5$, obtained if we assume identical contributions $\mathbf{L}_p = \mathbf{L}_n$ from the proton and neutron orbital angular momenta and no contribution from spin angular momenta.

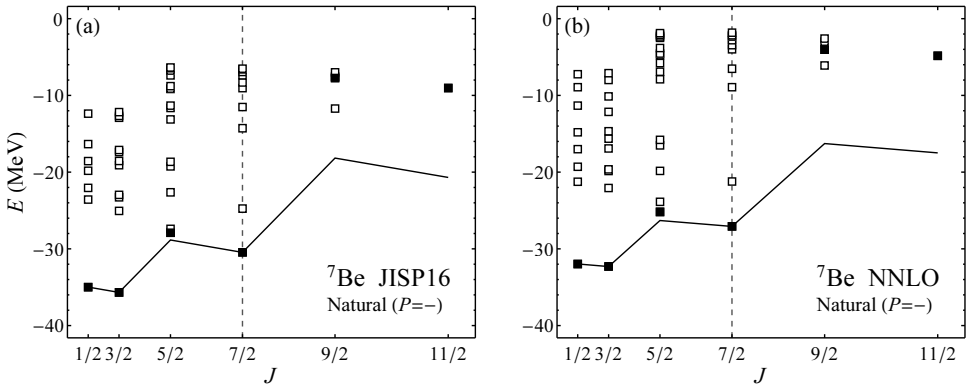

Fig. 9. Energy eigenvalues for states in the natural parity space of ^{7}Be, as obtained with the JISP16 (left) and NNLO (right) nucleon-nucleon interactions. See Fig. 5 caption for discussion of plot contents and labeling. From calculations with $N_{\max} = 10$ at $\hbar\omega = 20\,\mathrm{MeV}$.

to-next-to-next-to-leading-order (N^{3}LO) chiral interaction.[17] It is found that the dominant contribution to the ground state wave function arises from the $(4, 0)$ irreducible representation (irrep) of SU(3), paired with intrinsic spin contributions which all vanish, *i.e.*, $(S_p, S_n, S) = (0, 0, 0)$. The $(4, 0)$ irrep of SU(3) contains angular momentum states with $L = 0$, 2, and 4, corresponding to a truncated $K = 0$ rotational band.

To briefly summarize these observations, from the *ab initio* calculations there are clear and consistent indications of rotation, in the simplest example of ^{8}Be, based on patterns in energies and electromagnetic observables. The $K = 0$ ground state band is qualitatively consistent with an α-α structure, but discontinuities in observables at the maximal valence angular momentum suggest that the spherical shell structure (and shell model p-shell description) may retain physical relevance.

4.2. *Rotation in* ^{7}Be

The most distinctive and well-developed rotational band structures are observed in calculations for odd-mass nuclei. Given the same range of excitation energies and angular momenta, the low-lying $\Delta J = 1$ bands in the odd-mass nuclei provide a richer set of energy and electromagnetic observables. Yrast and near-yrast states yield the most immediately recognizable sets of candidate band members, so our focus will be on these states. The rotational bands in ^{7}Be (this section) and ^{9}Be (Sec. 4.3) serve as illustrative cases. Experimental counterparts for these calculated rotational bands may be identified.[14,29,40,41]

The low-lying levels calculated in ^{7}Be are shown in Fig. 9. A $K = 1/2$ yrast band is identified, again through a combination of rotational energies and collectively enhanced transition strengths. The quadrupole transitions, shown in Fig. 10, obey the characteristic pattern for a $K = 1/2$ band implied by the rotational model

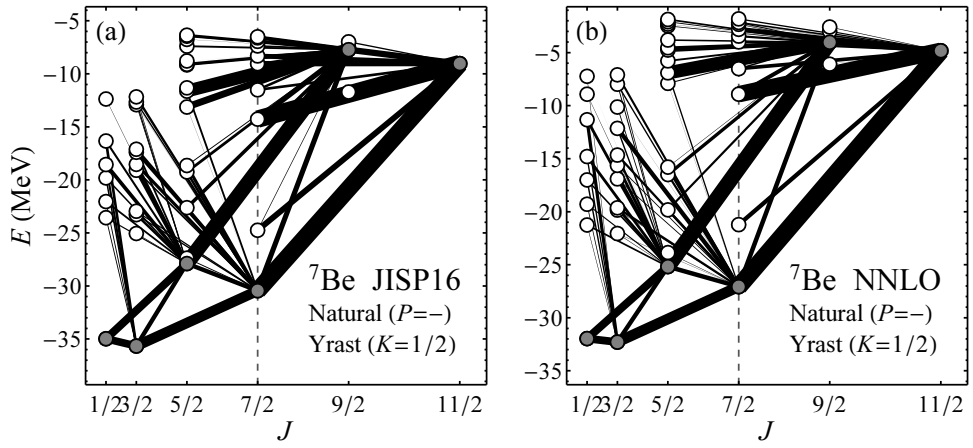

Fig. 10. Electric quadrupole transition strengths among levels in the ^{7}Be natural parity space, originating from yrast band members, as obtained with the JISP16 (left) and NNLO (right) nucleon-nucleon interactions. See Fig. 6 caption for discussion of plot contents and labeling. From calculations with $N_{\max} = 10$ at $\hbar\omega = 20\,\mathrm{MeV}$, using the proton quadrupole tensor.

[Fig. 3(b)]: stronger $\Delta J = 2$ transitions and comparatively weak (though still collective) $\Delta J = 1$ transitions. The energy staggering is such that the $J = 1/2$, $5/2$, ... levels are raised in energy, and the $J = 3/2$, $7/2$, ... levels are lowered (this direction for the staggering corresponds to a negative value of the Coriolis decoupling parameter a). Note that the staggering is sufficiently pronounced that the two lowest-J band members are inverted, as is experimentally observed.

Comparing the calculated energies with the rotational formula (2), it may be seen that the energies of the band members through the highest angular momentum accessible in the valence space ($J = 7/2$) are reasonably consistent with the rotational formula. (The line in Fig. 9 represents the predictions of the rotational formula, with band energy parameters E_0, A, and a extracted from the energies of the three lowest-energy band members, *i.e.*, $J = 1/2$, $3/2$, and $7/2$.) Although a second $J = 5/2$ state lies within $\sim 1\,\mathrm{MeV}$ of the yrast $J = 5/2$ state, in both calculations, the lack of enhanced transitions (Fig. 10) suggests negligible mixing of this "spectator" state with the yrast band member.

At higher angular momenta, $J = 9/2$ and $11/2$ states are calculated to have collective quadrupole transitions (Fig. 10) to the lower band members, suggesting their inclusion as band members. The energy staggering is such that the $J = 9/2$ band member lies off the yrast line. (Intriguingly, these states also have enhanced transitions to certain other, high-lying $J = 5/2$ and $7/2$ states, at excitation energies which seem to be roughly consistent between the JISP16 and NNLO calculations.) While the energies of these states lie above the rotational expectation (Fig. 9), these energies are also converging downward more rapidly than those of the lower band members, much as seen above for the $J = 6$ band member in ^{8}Be (Sec. 4.1).

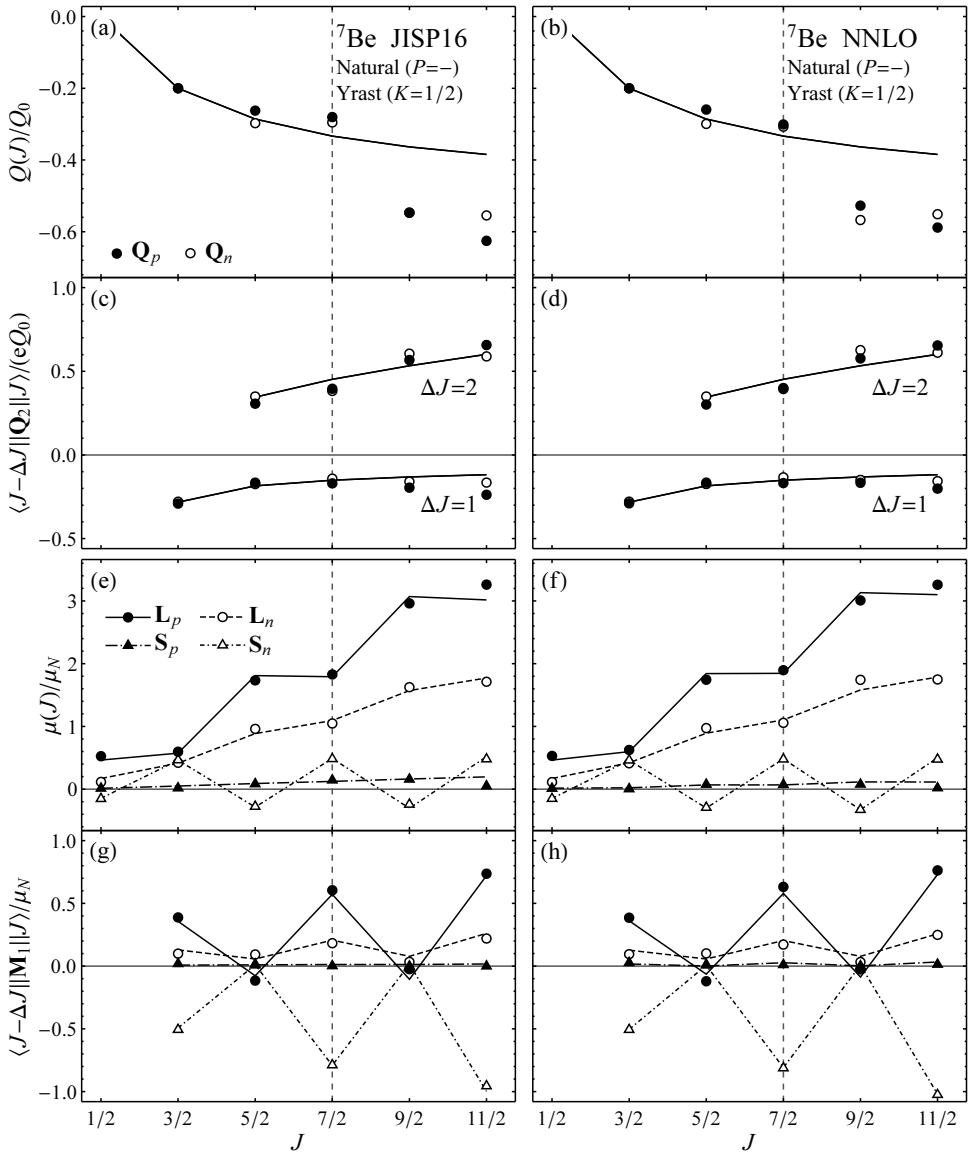

Fig. 11. Quadrupole and dipole matrix element observables for the ^{7}Be natural parity yrast band: quadrupole moments (first row), quadrupole transition reduced matrix elements (second row), dipole moments (third row), and dipole transition reduced matrix elements (fourth row), as obtained with the JISP16 (left) and NNLO (right) nucleon-nucleon interactions. See Fig. 8 caption for discussion of plot contents and labeling. From calculations with $N_{\max} = 10$ at $\hbar\omega = 20\,\mathrm{MeV}$.

A detailed test of the rotational description for these candidate ^{7}Be band members is obtained by comparing the many electric quadrupole moments and transition matrix elements among these states with the rotational expectation from (3)

and (4), as shown in the upper two rows of Fig. 11. Recall that only a single normalization constant, the intrinsic quadrupole moment Q_0, enters into the rotational predictions for the electric quadrupole moments and transitions, which are shown normalized to Q_0 in Fig. 11. (We have fixed Q_0 based on the lowest nonvanishing quadrupole moment, that of the $J = 3/2$ state.) Beyond this choice of normalization, agreement or disagreement of the *ab initio* calculated values with the rotational curves is entirely a test of the rotational picture. Quadrupole moments in Fig. 11 are calculated using both the proton (solid symbols) and neutron (open symbols) quadrupole tensors (Sec. 3). The proton and neutron quadrupole moments are normalized separately, since no *a priori* relation exists between the intrinsic matrix elements of the $\mathbf{Q}_p$ and $\mathbf{Q}_n$ operators. (In some cases, data points for the neutron and proton results may not be separately visible in these figures, when the values are so close as to be indistinguishable.)

We may observe an essentially similar behavior to that noted earlier for quadrupole observables in the ^{8}Be yrast band (Sec. 4.1), though now with the added richness of $\Delta J = 1$ transitions. The quadrupole moments [Fig. 11 (first row)] are consistent with a rotational picture up to the maximal valence angular momentum $J = 7/2$. There is again a modest discontinuity in the quadrupole moments (increasing by about half again over the rotational expectation) above this angular momentum. Although the $N_{\max}$ dependence is not shown in Fig. 11, the values of these quadrupole moments (even relative to those of the rest of the band, *i.e.*, normalized to Q_0) are poorly converged with $N_{\max}$. The quadrupole transition matrix elements [Fig. 11 (second row)] remain largely consistent with the rotational expectations throughout the candidate band, up to $J = 11/2$.

Likewise, note the remarkable level of consistency between the JISP16 [Fig. 11 (left)] and NNLO [Fig. 11 (right)] calculations of these observables. The similarity of these calculations lies not just in their mutual overall agreement with the rotational predictions, but in the nature of their deviations from the rotational formula and the sense of the splittings between the values of proton and neutron matrix elements (excepting, perhaps, certain details for the highest-J band members).

The calculations in Fig. 11 test not just the magnitudes of the moments and matrix elements, but also their signs. There are some ambiguities in the rotational predictions for the signs of the reduced matrix elements, due to the arbitrary phases entering into the definition of each eigenstate of a Hamiltonian operator (or, equivalently, the arbitrary overall sign arising on each eigenvector obtained in the numerical diagonalization of a Hamiltonian matrix). However, even once phase ambiguities are taken into account, a rich set of predicted correlations between signs of matrix elements for electric quadrupole ($\Delta J = 1$ and $\Delta J = 2$) and magnetic dipole transitions remains, as detailed in Sec. III C of Ref. 14. Since moments are deduced from *diagonal* matrix elements of the transition operator, they are invariant under the arbitrary sign choices in the definitions of eigenstates. The sign of a transition

matrix element varies with the sign choices on the initial and final states, σ_J and $\sigma_{J'}$, respectively, as the product $\sigma_{J'}\sigma_J$.

Matching a small subset of the *ab initio* calculated transition matrix elements (say, the $\Delta J = 1$ proton quadrupole matrix elements) to the signs conventionally adopted in the rotational description (Fig. 3) suffices to completely fix arbitrary signs. It is then meaningful to compare the signs of all other transition matrix elements — the proton and neutron quadrupole matrix elements, and all magnetic dipole terms — with the rotational predictions. The signs obtained in the *ab initio* calculations of Fig. 11 are uniformly consistent with the rotational picture.

We turn now to comparing the many magnetic dipole moments and transition matrix elements among these states with the rotational expectation from (6), as shown in the lower two rows of Fig. 11. The four distinct "dipole moments" calculated for each band member in ^{7}Be, obtained with the four different dipole terms, are shown in Fig. 11 (third row), while the four distinct sets of $\Delta J = 1$ dipole transition matrix elements are shown in Fig. 11 (fourth row). The lines indicate the rotational predictions from (6), with parameters determined to provide a best fit to the calculated moments and transitions (specifically, considering the band members with $J \leq 7/2$). These parameters are determined independently, for each dipole term operator (and, of course, for the calculations with different interactions).

Recall that there are only three parameters in the rotational predictions (6). The core gyromagnetic ratio g_R is responsible for the overall linear trend in the dipole moments, which is the dominant contribution for the orbital dipole terms [circles in Fig. 11 (third row)]. Then, for a $K = 1/2$ band, there are two relevant intrinsic matrix elements, where the second of these, or cross term in (6), contributes the staggering of the values as a function of J. Thus, there are only three parameters but many more (eleven) calculated values (for each dipole term and for each calculation in Fig. 11), and the *ab initio* calculated values appear to be highly consistent with a rotational pattern. Moreover, the senses of the deviations which do arise appear to be remarkably consistent between the JISP16 and NNLO calculations. Notice the near-vanishing proton spin contributions — these would be consistent, for instance, with a structure in which proton spins are paired to yield zero total proton spin angular momentum.

The rotational formula for magnetic dipole moments and transition matrix elements provided by (6) is the result of the classic rotational interpretation, formulated for heavier nuclei. As noted in Sec. 3, the basic assumption is that the nucleus separates into a deformed rotating core and residual extra-core particles. However, consistency with a model does not imply that the model provides the sole successful description of the physical system, nor that the model uniquely provides the correct underlying physical interpretation. For ^{7}Be, in particular, it might be natural, in a cluster description, to consider the nucleus either as an α-^{3}He dimer or as ^{8}Be coupled to a neutron hole.[28]

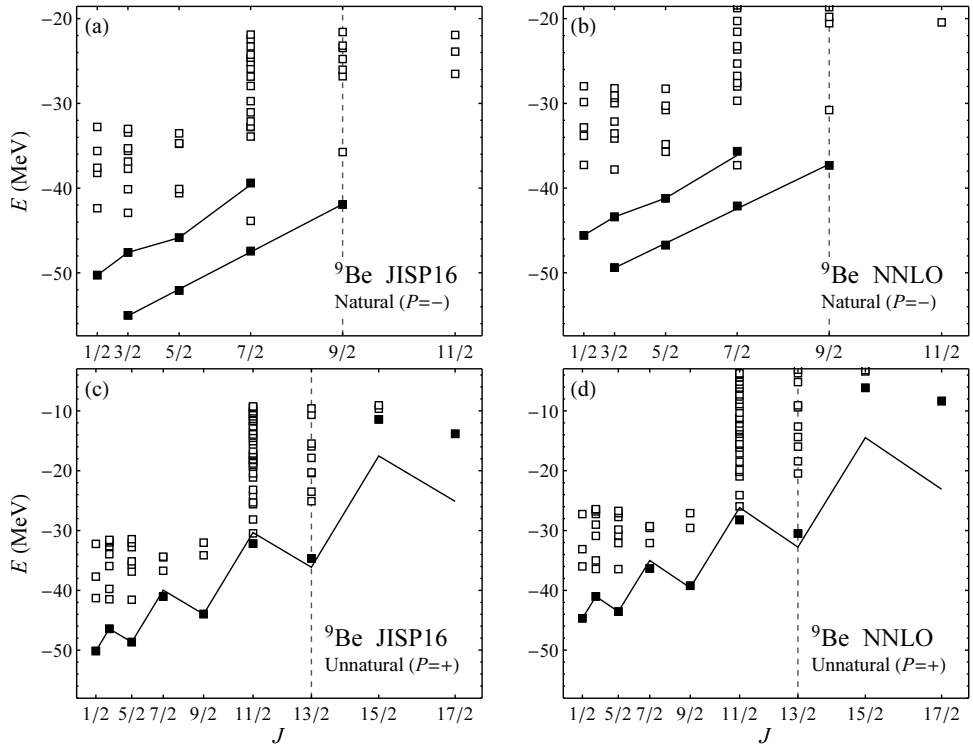

Fig. 12. Energy eigenvalues for states in the natural parity space of ^{9}Be (top) and unnatural parity space of ^{9}Be (bottom), as obtained with the JISP16 (left) and NNLO (right) nucleon-nucleon interactions. See Fig. 5 caption for discussion of plot contents and labeling. From calculations with $N_{\max} = 10$ (for natural parity) and $N_{\max} = 11$ (for unnatural parity) at $\hbar\omega = 20\,\mathrm{MeV}$.

4.3. *Rotation in* ^{9}Be

The isotope ^{9}Be has a natural interpretation in a cluster picture, as consisting of ^{8}Be plus a neutron, that is, as an α-α dimer with a covalent neutron shared between the α clusters.[28] Although the ground state is stable, all excited states are resonances, lying above the $\alpha + \alpha + n$ decay threshold.[29] The unnatural (positive) parity states begin at low excitation energy relative to the natural (negative) parity states: the ground state is $3/2^-$, but the first excited state, at an excitation energy of under 2 MeV, is $1/2^+$. We therefore show, in Fig. 12, the energies of the eigenstates obtained in both the natural [Fig. 12 (top)] and unnatural [Fig. 12 (bottom)] parity spaces.

Based both on energies and transition strengths, two low-lying bands are identified in the natural parity space, both for the JISP16 [Fig. 12(a)] and NNLO [Fig. 12(b)] interactions: an yrast $K = 3/2$ band (with $J = 3/2$, $5/2$, $7/2$, and $9/2$ members) and an excited $K = 1/2$ band (with $J = 1/2$, $3/2$, $5/2$, and $7/2$ members). A similar pattern of low-lying states may be found in traditional shell model

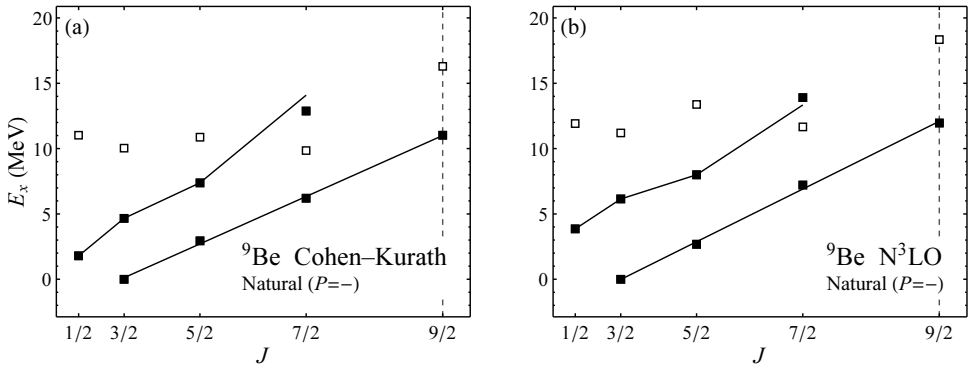

Fig. 13. Excitation energies for states in the natural parity space of ^{9}Be, for comparison with Fig. 12 (top), as obtained in: (a) a valence shell model calculation using the Cohen-Kurath interaction and (b) an NCCI calculation with the N^{3}LO interaction. Calculations from Ref. 18.

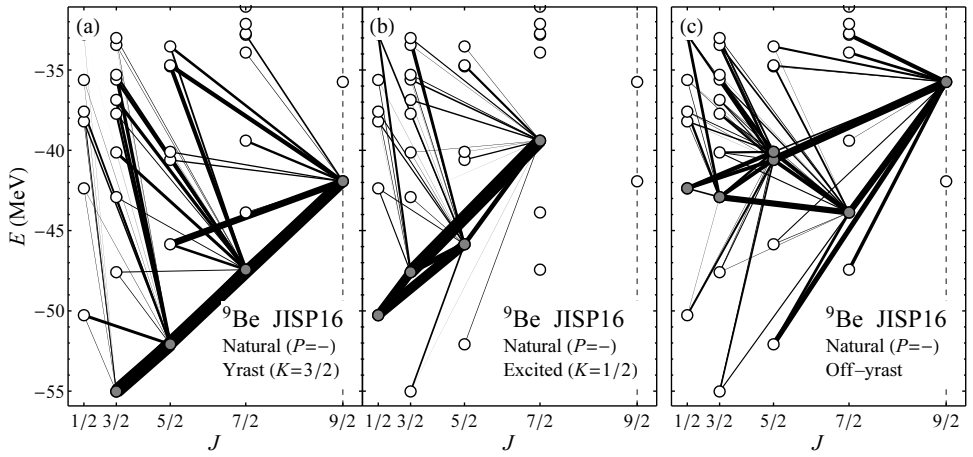

Fig. 14. Electric quadrupole transition strengths among levels in the ^{9}Be natural parity space, orignating from (a) yrast band members, (b) excited band members, and (c) selected off-yrast states (see text), as obtained with the JISP16 nucleon-nucleon interaction. See Fig. 6 caption for discussion of plot contents and labeling. From calculations with $N_{\max} = 10$ at $\hbar\omega = 20\,\mathrm{MeV}$, using the proton quadrupole tensor.

calculations with the phenomenological Cohen-Kurath p-shell interaction,[42] shown in Fig. 13(a). (The maximal angular momentum accessible within the valence space is $J = 9/2$.) The apparent restriction of these bands to the valence space (although enhanced quadrupole transitions to off-yrast states at higher J are not excluded) and consistency with p-shell calculations would seem to suggest that the structure of these bands can be largely described by dynamics within the valence shell. As a further indication of the robustness of the rotational structure, similar results from NCCI calculations with the N^{3}LO interaction are shown in Fig. 13(b).

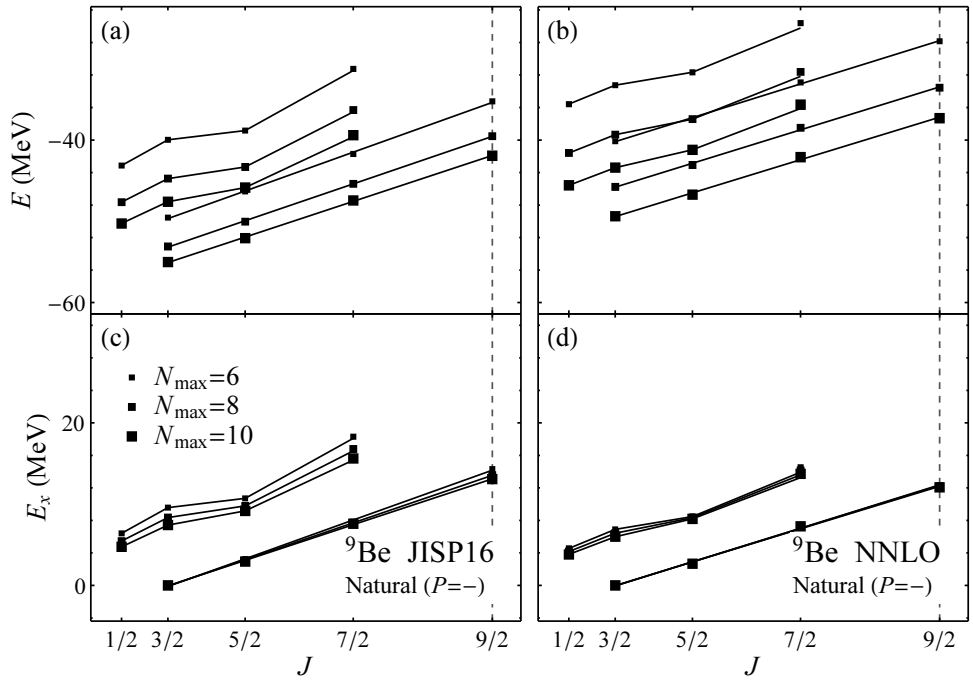

Fig. 15. Dependence of calculated energies for ^{9}Be natural parity yrast and excited band members on $N_{\max}$: energy eigenvalues E (top) and excitation energies E_x (bottom), as obtained with the JISP16 (left) and NNLO (right) nucleon-nucleon interactions. See Fig. 5 caption for discussion of plot contents and labeling. From calculations with $N_{\max} = 6$, 8, and 10 at $\hbar\omega = 20\,\mathrm{MeV}$.

The quadrupole transition strengths from the band members are shown in Fig. 14(a,b). The band assignments are based on enhanced transitions within each band. There is also one example of an enhanced cross transition between the bands (namely, from the $J = 9/2$ terminating band member of the $K = 3/2$ band to the $J = 5/2$ member of the excited band).

It is intriguing that the $J = 7/2$ member of the excited band is the *third* $J = 7/2$ state, in all four calculations considered here, *i.e.*, with JISP16 [Fig. 12(a)], NNLO [Fig. 12(b)], Cohen-Kurath [Fig. 13(a)], and N^{3}LO [Fig. 13(b)] interactions. The "spectator" $7/2^-_2$ state, rather than being part of the rotational band structures, appears to be part of a grouping of off-yrast states connected by enhanced quadrupole transitions, as shown in Fig. 14(c). This grouping is comprised also of the next off-yrast $J = 1/2$, $3/2$, $5/2$ (both members of a close doublet), and $9/2$ states. The W-shaped staggering pattern in the energies of these off-yrast states (raised $1/2$, $5/2$, and $9/2$ members) is consistent across all four calculations.

To provide a foundation for the rotational description of ^{9}Be and to lay the groundwork for our discussion of the band energy parameters below (Sec. 5), the $N_{\max}$ dependence of the energies for the yrast and excited band members is in-

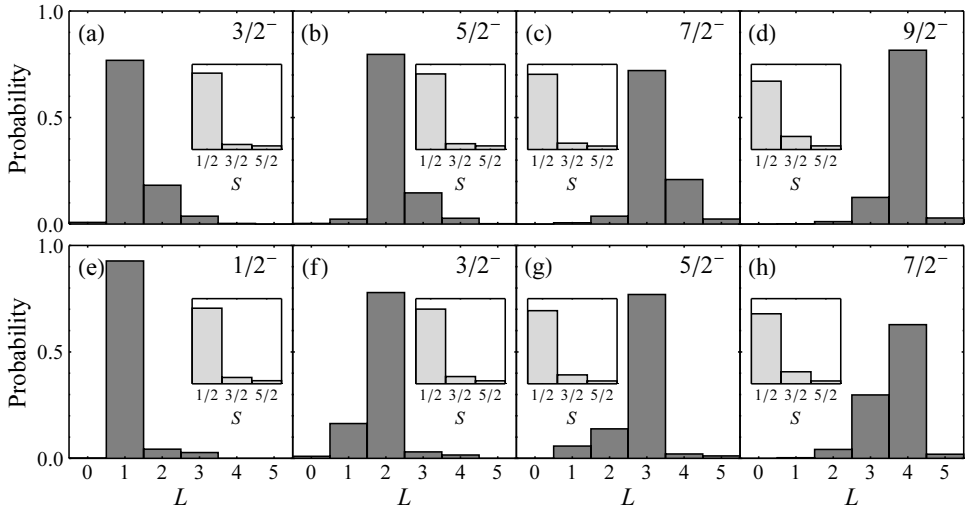

Fig. 16. Decomposition of ^{9}Be natural parity yrast (top) and excited (bottom) band members according to orbital angular momentum L and spin angular momentum S (insets), for the N^{3}LO interaction. Calculations from Ref. 18.

vestigated in Fig. 15. Much as we have already seen for the yrast band in ^{8}Be (Fig. 7), the calculated energy eigenvalues shift lower by several MeV with each step in $N_{\max}$ [Fig. 15 (top)], while the relative energies within the band remain comparatively unchanged, as may be seen more directly from the excitation energies [Fig. 15 (bottom)]. The excitation energy of the excited band relative to the yrast band, though not converged, varies much less rapidly with $N_{\max}$ than do the eigenvalues themselves.

The magnetic dipole observables can provide some insight into the angular momentum structure of a rotational band (Secs. 4.1 and 4.2). However, the angular momentum structure may also be explored more directly, by decomposing the eigenfunctions into components of good orbital angular momentum L and/or spin S (which may be further subdivided into proton and neutron spins, S_p and S_n). This decomposition is accomplished automatically if the eigenproblem is solved from the beginning in a basis of good orbital and spin angular momentum quantum numbers, as in the SU(3)-coupled NCCI code of Dytrych *et al.*[43] However, this decomposition may alse be extracted from wave functions obtained in conventional M scheme NCCI calculations, as described in Ref. 18 (via the so-called "Lanczos trick").

The angular momentum and spin decompositions for the natural parity yrast and excited band members in ^{9}Be are shown in Fig. 16. It is apparent that each state is dominated by a specific L component and by an intrinsic spin $S = 1/2$. That is, the calculated wave functions approximately obey an LS coupling scheme.[28] (The angular momentum decomposition for rotational states in ^{7}Li, the mirror nucleus to ^{7}Be, is also explored in Ref. 18 and yields similarly strong evidence of LS coupling.)

The LS coupling, while reasonably pronounced in Fig. 16, is not pure. In fact, the mixture of L components in the *ab initio* calculated ground state [Fig. 16(a)] is consistent with a simple single-irrep SU(3) shell-model description, including spin-orbit interaction, as presented in Ref. 39: an $L = 1$ contribution of $21/26 \approx 81\%$ and an $L = 2$ contribution of $5/26 \approx 19\%$.

In both bands, the dominant L values for successive band members are found to be $L = 1$, 2, 3, and 4. In the yrast band, the angular momenta are coupled in the "stretched" (or "aligned") sense, with $J = L+1/2$, while, in the excited band, these same angular momenta are coupled in the "unstretched" (or "antialigned") sense, with $J = L - 1/2$. This pattern may be interpreted in a core-particle rotational picture, in which the core orbital motion generates a $K = 1$ band, which then couples to the neutron spin, in aligned and antialigned senses, to generate a $K = 3/2$ band and a $K = 1/2$ band, respectively.

Finally, we note that the calculated yrast states of the *unnatural* parity space of ^{9}Be also constitute a $K = 1/2$ rotational band, with candidate band members at least through $J = 17/2$ [Fig. 12 (bottom)]. The maximal angular momentum possible in the lowest shell model unnatural parity space (the space of $1\hbar\omega$ excitations) or, equivalently, the NCCI $N_{\max} = 1$ space is $J = 13/2$ [dashed vertical lines in Fig. 12 (bottom)]. The properties of this unnatural parity band are similar to those already discussed for the calculated ^{7}Be yrast $K = 1/2$ band (electromagnetic observables are not shown here, but see Fig. 8 of Ref. 14): (i) band members above the maximal valence angular momentum lie above the rotational prediction in energy but are converging downward in energy relative to the lower band members, (ii) quadrupole moments and transitions are in close agreement with the rotational predictions, except for an enhancement in quadrupole moments relative to the rotational formula above the maximal valence angular momentum, and (iii) dipole moments and transitions are generally consistent with the rotational predictions through the highest J considered, including above the maximal valence angular momentum.

5. Extrapolation of energies and prediction of rotational band parameters

Returning to the initial questions, from Sec. 1, now that we have explored how *recognizable* the signatures of rotation are, seen that they are surprisingly *robust* across interactions (and despite limitations in convergence), and inquired into aspects of the intrinsic *physical structure*, let us touch upon how the emergent rotation compares to experiment in quantitative detail.

The energy parameters for the bands in $^{7-9}$Be, as extracted from level energies in the *ab initio* calculations, are summarized in Fig. 17. Recall that the band energy parameter E_0, rotational parameter A, and Coriolis decoupling parameter a (for $K = 1/2$) entering into the rotational energy formula (2) represent the "height" of the band, the "slope" of the band, and the "staggering" of the band, respectively,

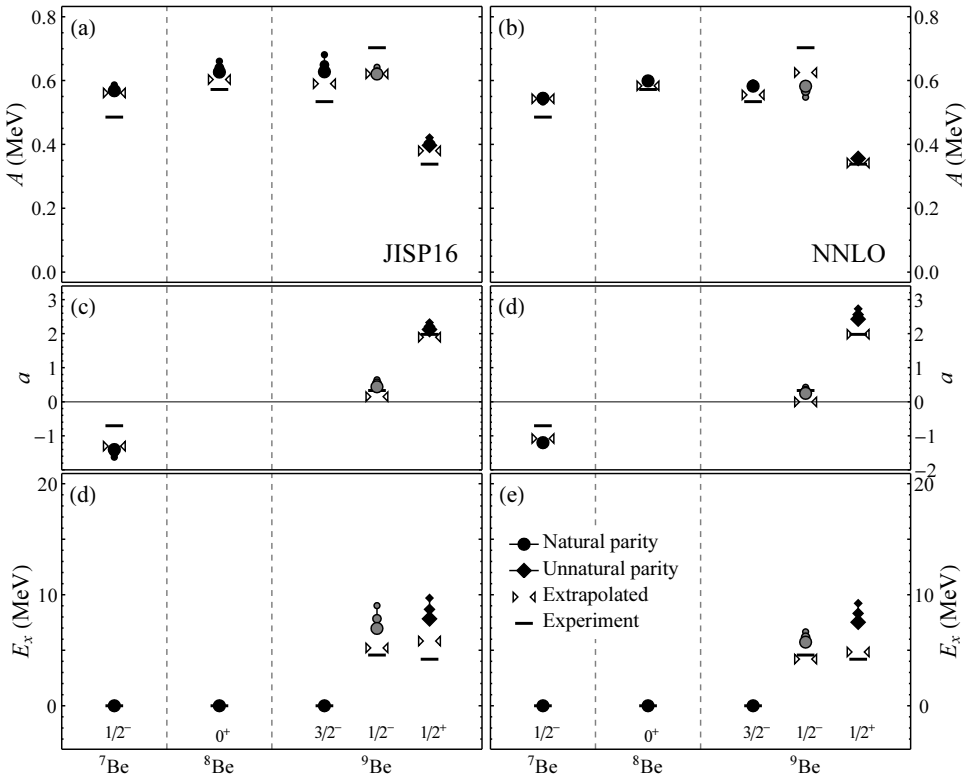

Fig. 17. Band energy parameters for $^{7-9}$Be: the rotational constant A (top), Coriolis decoupling parameter a (middle), and band excitation energy E_x (bottom), as obtained with the JISP16 (left) and NNLO (right) nucleon-nucleon interactions. Values are shown for $N_{\max} = 6$, 8, and 10 (for natural parity) or $N_{\max} = 7$, 9, and 11 (for unnatural parity), with larger symbols for higher $N_{\max}$ values. Parameter values are also shown based on exponentially extrapolated level energies (paired triangles) and from the experimentally observed levels (horizontal lines).

in a plot of energies *vs.* $J(J+1)$ (*e.g.*, Figs. 5 and 9). The band excitation energy E_x, shown in Fig. 17 (bottom), is defined relative to the yrast band energy as $E_x \equiv E_0 - E_{0,\mathrm{yrast}}$.[g] Results are shown for a sequence of $N_{\max}$ truncations. Parameters for the experimentally observed bands (based on the set of experimental levels detailed in Ref. 14) are also shown (horizontal lines).

Ideally, comparison of the calculated and experimental band parameters pro-

[g]Note that the *band energy* parameter E_0 is the energy intercept of the band at $J = 0$. It is therefore *not* equivalent to the *band head energy* (except perhaps in the case of a $K = 0$ band). Likewise, the *band excitation energy*, as the difference of two such band energy parameters, is the vertical separation between the excited band and the yrast band as they intersect the energy axis at $J = 0$. It is therefore *not* to be conflated with the *band head excitation energy* (the two being equivalent only in the case where both bands are even-spin $K = 0$ bands, thus both with $J = 0$ band heads, and even then only in the ideal case that the band member energies lie exactly on the rotational line).

vides a direct test of the degree to which the nuclear many-body problem with the chosen internucleon interaction (here, JISP16 or NNLO) reproduces the rotational dynamics actually occurring in the physical Be isotopes. This comparison is subject to various challenges: the computational limitations in obtaining convergence of energies (already discussed), the experimental challenge of identifying the band members (in some cases from amongst broad, overlapping resonances, with limited information available for spin-parity assignments and almost exclusively without electromagnetic decay data[29,40]), ambiguity in describing the band through band energy parameters when level energies deviate from the rotational formula, and the more fundamental consideration that some of the levels involved are broad resonances for which an equivalent sharp bound state energy is not well-defined.

Nonetheless, the calculated band parameters in Fig. 17 are sufficiently stable with respect to $N_{\max}$ (and the experimental band parameters sufficiently well-defined) to permit a meaningful comparison. The experimental values of the rotational parameter A [Fig. 17 (top)] for the various bands vary by about a factor of 2, from ~ 0.5–$0.7\,\mathrm{MeV}$ for the experimental natural parity bands down to $\sim 0.34\,\mathrm{MeV}$ for the ^{9}Be unnatural parity band. The JISP16 and NNLO calculations both consistently yield rotational parameters of $\sim 0.6\,\mathrm{MeV}$ for the natural parity bands and ~ 0.35–$4\,\mathrm{MeV}$ for the ^{9}Be unnatural parity band. The Coriolis staggering for the calculated $K = 1/2$ bands [Fig. 17 (middle)] varies in both amplitude and sign, and the experimental trend in both these properties is reproduced across the bands.

The excitation energies for the excited natural parity band and the unnatural parity band in ^{9}Be [Fig. 17 (bottom)] are decreasing with $N_{\max}$ [recall Fig. 15 (bottom)], bringing them toward the experimental values. Yet, they are varying too strongly with $N_{\max}$ for it to be immediately obvious how close the converged predictions will lie to the experimental values.

One may attempt to overcome incomplete convergence — and obtain more precise comparisons with the experimentally identified rotational bands — by application of basis extrapolation methods.[44,45] If the functional dependence (on $N_{\max}$ and $\hbar\omega$) were known, describing how the energy eigenvalues calculated in the truncated spaces approach their converged values, it should, in principle, be possible to take unconverged values obtained from calculations in truncated spaces and use them to estimate the true converged eigenvalues. Such methods are still in their formative stages. Nonetheless, it is intriguing to apply a straightforward scheme based on a presumed exponential convergence of energy eigenvalues with $N_{\max}$:[46,47]

$$E(N_{\max}) = c_0 + c_1 \exp(-c_2 N_{\max}). \tag{8}$$

Calculations of the energy at three successive $N_{\max}$ values, for fixed $\hbar\omega$, are sufficient to determine all three parameters c_i in (8). Extrapolating to the limit $N_{\max} \to \infty$ gives $E(N_{\max}) \to c_0$, so the fitted value for c_0 provides an estimate of the converged value for the energy. The results of this procedure are typically most stable when $\hbar\omega$ is taken near the variational minimum in the energy curves as functions of $\hbar\omega$,[47] as in Figs. 2(a,b), *i.e.*, $\hbar\omega \approx 20$–$25\,\mathrm{MeV}$ for the isotopes and interactions considered

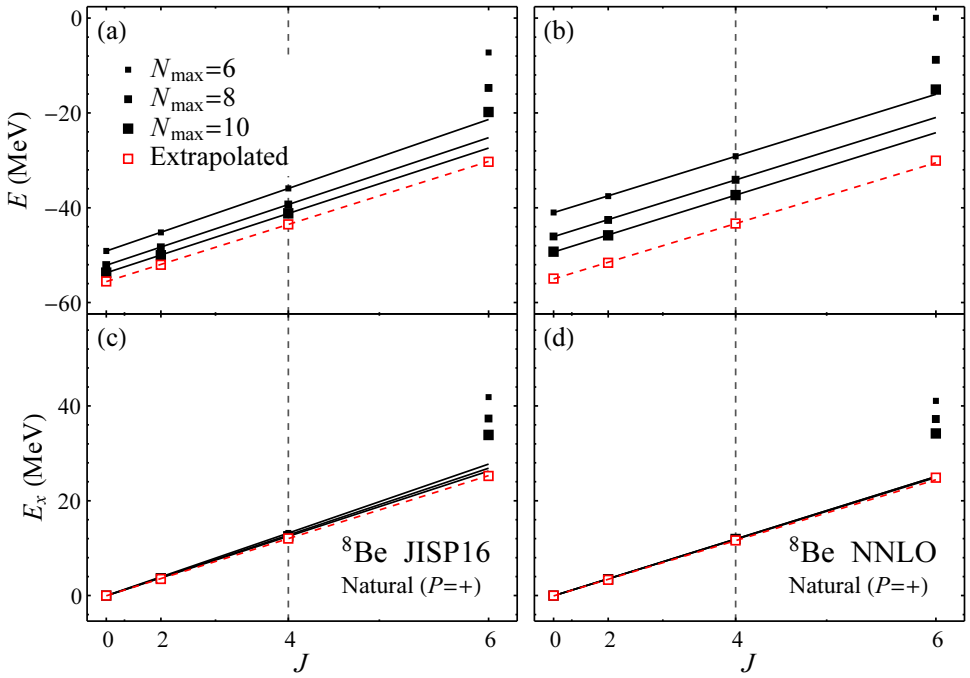

Fig. 18. Calculated energy eigenvalues E (top) and excitation energies E_x (bottom), for ^{8}Be natural parity yrast band members, from calculations with $N_{\max} = 6$, 8, and 10, as in Fig. 5, together with the exponentially extrapolated eigenvalues (top) and corresponding excitation energies (bottom).

here (see Ref. 47 for further discussion of the procedure).

To apply this exponential extrapolation scheme to our rotational analysis, we must first extrapolate the energies of the individual band members. Let us take the ^{8}Be yrast band for illustration, and revisit the $N_{\max}$ dependence of the calculated values from Fig. 5. The result of exponentially extrapolating these values is seen in Fig. 18 (open symbols). Observe that the energy of the $J = 6$ band member comes into line with the rotational predictions. Rotational energy parameters are then obtained by matching the rotational energy formula (2) to the extrapolated level energies (dashed lines in Fig. 18).

The band energy parameters for $^{7-9}$Be obtained from such extrapolations are shown in Fig. 17 (paired triangles), providing a more concrete estimate of where the converged values lie. Note in particular the reproduction of the excitation energies for both excited bands in ^{9}Be (at the MeV scale), as well as the reproduction of the unnatural parity band rotational and Coriolis parameters. This success is to be contrasted with the apparent failure to reproduce the exceptionally high experimental rotational parameter value of ~ 0.7 MeV for the natural parity excited band. However, the exponential extrapolations are subject to considerable uncertainties,[47]

and several of the experimental levels (including in the ^{9}Be natural parity excited band) are subject to significant ambiguitities.[29,48] It is therefore not yet clear to what extent the remaining discrepancies reflect actual deficiencies in the *ab initio* description of the nucleus with the chosen interactions, as opposed to these other limitations.

6. Conclusions

Through illustrative examples of rotational bands in *ab initio* NCCI calculations for $^{7-9}$Be, we have seen how the emergence of rotational structure can be recognized through a combination of rotational energy patterns, enhanced electric quadrupole strengths, and general agreement of electric quadrupole and magnetic dipole moments and transition matrix elements with rotational predictions.

It is simplest to recognize rotational states near the yrast line, where the density of states is comparatively low, as in the bands considered here. However, rotational structure may also be recognized in states further away from the yrast line (see the excited $K = 0$ band of ^{10}Be,[41,49,50] as calculated and discussed in Ref. 14). It is also most straightforward to recognize rotational states with angular momenta accessible within the traditional valence space (or NCCI $N_{\max} = 0$ or 1 space), since energies of band members above this angular momentum may have significantly different convergence properties and may deviate from the rotational formula, at least in the computationally-accessible truncated calculations.

We have also begun to develop a sense of the robustness of the emergent rotation in *ab initio* calculations: at a more fundamental level, how robustly the imperfectly-known internucleon interaction can be expected to give rise to rotation, and, at a more pragmatic level, how robust the rotation is in incompletely-converged many-body calculations carried out in truncated spaces.

We observe a remarkable similarity in spectral details across results obtained with two independently-derived interactions: the JISP16 interaction, obtained by inverse-scattering methods, and the chiral NNLO interaction $\mathrm{NNLO_{opt}}$ (calculations with a chiral N^{3}LO interaction were also considered). The similarity lies not only in the presence of analogous rotational bands across the calculations but in the subtle deviations of these bands from the ideal rotational formulas (*e.g.*, Fig. 11). The similarities arise despite the different levels and rates of convergence — compare, *e.g.*, the energies in Fig. 7(a) with those in Fig. 7(b). Comparing the predictions for band energy parameters obtained with these two interactions, we found a high level of quantitative consistency (Fig. 17). Here, a simple exponential basis extrapolation scheme for energy eigenvalues aided the comparison of the less-converged observables (*e.g.*, certain band excitation energies), but, for most of the band energy parameters, the consistency is apparent even without need for extrapolation.

It is particularly valuable here to note consistency across methods. Although the focus of this review is on NCCI calculations, quantum Monte Carlo calculations

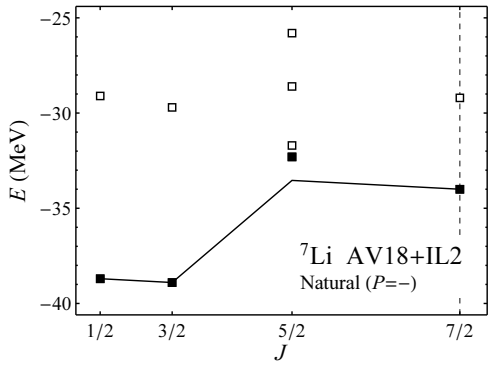

Fig. 19. Energy eigenvalues for states in the natural parity space of ^{7}Li (the mirror nucleus to ^{7}Be), as obtained in Green's Function Monte Carlo (GFMC) calculations with the AV18 nucleon-nucleon and IL2 three-nucleon interactions, for comparison with Fig. 9. Calculations from Ref. 1.

of ^{7}Li (the mirror nucleus to ^{7}Be), as shown in Fig. 19, also readily reproduce an 3/2-1/2-7/2-5/2 yrast angular momentum sequence,[1] reflective of a $K = 1/2$ band with negative Coriolis staggering. These calculations were carried out with an internucleon interaction consisting of an AV18 two-body part[51] and an IL2 three-body part.[52] It is intriguing to note the detailed resemblance of the eigenvalue spectrum in Fig. 19 to the NCCI calculations of Fig. 9. Again the $J = 5/2$ band member lies slightly higher than the rotational formula would give, based on the $J = 1/2$, 3/2, and 7/2 states. The same pattern of off-yrast states arises, as well: the close $J = 5/2$ doublet and a subsequent set of off-yrast states ($J = 1/2$, 3/2, 5/2, and 7/2) with the same staggering pattern as in Fig. 9.

The rotational patterns are also perhaps surprisingly robust against truncation of the many-body calculation. The principal challenge in identifying collective structure in NCCI calculations is the weak convergence of many of the relevant observables (Fig. 2). However, there is an important distinction between convergence of individual observables, taken singly, and convergence of relative properties, such as excitation energies (and, especially, their ratios) or ratios of different electromagnetic matrix elements. It is these latter, relative properties that are essential to the recognition of rotation through comparison with the rotational formula.

Our initial focus in examining observables lay simply in recognizing rotational patterns in the *ab initio* calculations and examining their fidelity to the rotational formulas. The existence of such patterns suggests a *rotational separation* of the wave functions, as in (1). However, by itself, it leaves unanswered the question of the physical origin and *intrinsic structure* of the wave functions, *i.e.*, the nature of the intrinsic state $|\phi_K\rangle$. The two classic paradigms for understanding this structure are α clustering and p-shell dynamics, including SU(3) symmetry in the p shell. (A more comprehensive, multishell framework for understanding the emergence of collective deformation and rotational degrees of freedom is provided by $\mathrm{Sp}(3,\mathbb{R})$

symplectic symmetry.[53,54])

Traditionally, in rotational analysis, intrinsic matrix elements of the multipole operators are the essential source of information on intrinsic structure.[25] The electric quadrupole moments and transitions provide insight into the nuclear deformation. The absolute magnitudes of the quadrupole observables are unconverged in the NCCI calculations (leaving only the ratio $Q_{0,p}/Q_{0,n}$, which may provide insight into the relative deformation of the proton and neutron distributions, as discussed in Sec. IV B of Ref. 14). However, magnetic dipole intrinsic matrix elements probe the orbital and spin angular momentum structure of the rotational states, which may also be more directly examined through angular momentum (L, S, S_p, and S_n) decompositions of the wave functions.

From the examples considered here, it appears that the rotational bands in $^{7-9}$Be are consistent with an α-α clustered rotational core and particle-rotor descriptions. Nonetheless, discontinuities in observables at the maximal valence angular momentum suggest that the spherical shell structure also plays some role. It is not clear whether these discontinuities are transient artifacts of incomplete convergence in truncated calculations or instead persist to the full, untruncated many-body space. The preliminary indications vary depending upon the observables considered, *e.g.*, the quadrupole moments in Fig. 8 (top) or the excitation energies in Fig. 18 (bottom).

Finally, a quantitative comparison of the emergent *ab initio* rotation with experiment is subject to many challenges, from the computational side (convergence), the experimantal side (including identification of the relevant levels, lack of electromagnetic transition data, and resolution of broad resonances), and the more fundamental limitations to applying bound-state methods and a bound-state formulation of the rotational formalism to resonant states. Nonetheless, despite these challenges, we have seen that the band energy parameters extracted from *ab initio* calculations (Fig. 17) display a notable level of consistency, both qualitative and quantitative, when compared with those extracted from experiment.

Acknowledgements

Discussions with M. Freer, T. Dytrych, S. C. Pieper, and R. B. Wiringa are gratefully acknowledged. We thank C. W. Johnson for providing calculations from Ref. 18. This material is based upon work supported by the U.S. Department of Energy, Office of Science, under Award Numbers DE-FG02-95ER-40934, DESC0008485 (SciDAC/NUCLEI), and DE-FG02-87ER40371, and by the U.S. National Science Foundation, under Grant Number 0904782. An award of computer time was provided by the U.S. Department of Energy Innovative and Novel Comutational Impact on Theory and Experiment (INCITE) program. This research used resources of the National Energy Research Scientific Computing Center (NERSC) and the Argonne Leadership Computing Facility (ALCF), which are DOE Office of Science user facilities supported under Contracts DE-AC02-05CH11231 and DE-

AC02-06CH11357. Computational resources were also provided by the University of Notre Dame Center for Research Computing.

References

1. S. C. Pieper, R. B. Wiringa and J. Carlson, *Phys. Rev. C* **70** (2004) 054325.
2. T. Neff and H. Feldmeier, *Nucl. Phys. A* **738** (2004) 357.
3. G. Hagen, D. J. Dean, M. Hjorth-Jensen, T. Papenbrock and A. Schwenk, *Phys. Rev. C* **76** (2007) 044305.
4. S. Bacca, N. Barnea and A. Schwenk, *Phys. Rev. C* **86** (2012) 034321.
5. N. Shimizu, T. Abe, Y. Tsunoda, Y. Utsuno, T. Yoshida, T. Mizusaki, M. Honma and T. Otsuka, *Prog. Exp. Theor. Phys.* **2012** (2012) 01A205.
6. B. R. Barrett, P. Navrátil and J. P. Vary, *Prog. Part. Nucl. Phys.* **69** (2013) 131.
7. A. M. Shirokov, V. A. Kulikov, P. Maris and J. P. Vary, Bindings and spectra of light nuclei with JISP16, in *NN and 3N Interactions*, eds. L. D. Blokhintsev and I. I. Strakovsky (Nova Science, Hauppauge, N.Y., 2014) p. 511.
8. D. J. Rowe, *Nuclear Collective Motion: Models and Theory* (World Scientific, Singapore, 2010).
9. R. B. Wiringa, S. C. Pieper, J. Carlson and V. R. Pandharipande, *Phys. Rev. C* **62** (2000) 014001.
10. T. Dytrych, K. D. Sviratcheva, C. Bahri, J. P. Draayer and J. P. Vary, *Phys. Rev. C* **76** (2007) 014315.
11. T. Neff and H. Feldmeier, *Eur. Phys. J. Special Topics* **156** (2008) 69.
12. T. Dytrych, K. D. Launey, J. P. Draayer, P. Maris, J. P. Vary, E. Saule, U. Catalyurek, M. Sosonkina, D. Langr and M. A. Caprio, *Phys. Rev. Lett.* **111** (2013) 252501.
13. M. A. Caprio, P. Maris and J. P. Vary, *Phys. Lett. B* **719** (2013) 179.
14. P. Maris, M. A. Caprio and J. P. Vary, *Phys. Rev. C* **91** (2015) 014310.
15. A. M. Shirokov, J. P. Vary, A. I. Mazur and T. A. Weber, *Phys. Lett. B* **644** (2007) 33.
16. M. A. Caprio, P. Maris, J. P. Vary and R. Smith, *Rom. J. Phys.* **60** (2015) 738.
17. D. R. Entem and R. Machleidt, *Phys. Rev. C* **68** (2003) 041001.
18. C. W. Johnson, *Phys. Rev. C* **91** (2015) 034313.
19. P. Maris, H. M. Aktulga, M. A. Caprio, U. V. Catalyurek, E. Ng, D. Oryspayev, H. Potter, E. Saule, M. Sosonkina, J. P. Vary, C. Yang and Z. Zhou, *J. Phys. Conf. Ser.* **403** (2012) 012019.
20. P. Maris, H. M. Aktulga, S. Binder, A. Calci, Ü. V. Çatalyürek, J. Langhammer, E. Ng, E. Saule, R. Roth, J. P. Vary and C. Yang, *J. Phys. Conf. Ser.* **454** (2013) 012063.
21. P. Maris, J. P. Vary, A. Calci, J. Langhammer, S. Binder and R. Roth, *Phys. Rev. C* **90** (2014) 014314.
22. A. Ekström, G. Baardsen, C. Forssén, G. Hagen, M. Hjorth-Jensen, G. R. Jansen, R. Machleidt, W. Nazarewicz, T. Papenbrock, J. Sarich and S. M. Wild, *Phys. Rev. Lett.* **110** (2013) 192502.
23. M. Moshinsky and Y. F. Smirnov, *The Harmonic Oscillator in Modern Physics* (Harwood Academic Publishers, Amsterdam, 1996).
24. J. Suhonen, *From Nucleons to Nucleus* (Springer-Verlag, Berlin, 2007).
25. A. Bohr and B. R. Mottelson, *Nuclear Structure* (World Scientific, Singapore, 1998).
26. M. A. Caprio, P. Maris and J. P. Vary, *Phys. Rev. C* **90** (2014) 034305.
27. H. Iwasaki, T. Motobayashi, H. Akiyoshi, Y. Ando, N. Fukuda, H. Fujiwara, Z. Fülöp, K. Hahn, Y. Higurashi, M. Hirai, I. Hisanaga, N. Iwasa, T. Kijima, T. Minemura,

T. Nakamura, M. Notani, S. Ozawa, H. Sakurai, S. Shimoura, S. Takeuchi, T. Teranishi, Y. Yanagisawa and M. Ishihara, *Phys. Lett. B* **481** (2000) 7.
28. D. R. Inglis, *Rev. Mod. Phys.* **25** (1953) 390.
29. D. R. Tilley, J. H. Kelley, J. L. Godwin, D. J. Millener, J. E. Purcell, C. G. Sheu and H. R. Weller, *Nucl. Phys. A* **745** (2004) 155.
30. V. M. Datar, D. R. Chakrabarty, S. Kumar, V. Nanal, S. Pastore, R. B. Wiringa, S. P. Behera, A. Chatterjee, D. Jenkins, C. J. Lister, E. T. Mirgule, A. Mitra, R. G. Pillay, K. Ramachandran, O. J. Roberts, P. C. Rout, A. Shrivastava and P. Sugathan, *Phys. Rev. Lett.* **111** (2013) 062502.
31. P. Sternberg, E. G. Ng, C. Yang, P. Maris, J. P. Vary, M. Sosonkina and H. V. Le, Accelerating configuration interaction calculations for nuclear structure, in *SC '08: Proceedings of the 2008 ACM/IEEE Conference on Supercomputing*, (IEEE Press, Piscataway, NJ, 2008). Article No. 15.
32. P. Maris, M. Sosonkina, J. P. Vary, E. Ng and C. Yang, *Procedia Comput. Sci.* **1** (2010) 97.
33. H. M. Aktulga, C. Yang, E. G. Ng, P. Maris and J. P. Vary, *Concurrency Computat.: Pract. Exper.* **26** (2013) 2631.
34. R. R. Whitehead, A. Watt, B. J. Cole and I. Morrison, *Adv. Nucl. Phys.* **9** (1977) 123.
35. D. Kurath, *Phys. Rev.* **124** (1961) 552.
36. P. Maris and J. P. Vary, *Int. J. Mod. Phys. E* **22** (2013) 1330016.
37. J. P. Elliott, *Proc. R. Soc. London A* **245** (1958) 128.
38. M. Harvey, *Adv. Nucl. Phys.* **1** (1968) 67.
39. D. J. Millener, *Nucl. Phys. A* **693** (2001) 394.
40. D. R. Tilley, C. M. Cheves, J. L. Godwin, G. M. Hale, H. M. Hofmann, J. H. Kelley, C. G. Sheu and H. R. Weller, *Nucl. Phys. A* **708** (2002) 3.
41. H. G. Bohlen, W. von Oertzen, R. Kalpakchieva, T. N. Massey, T. Corsch, M. Milin, C. Schulz, Tz. Kokalova and C. Wheldon, *J. Phys. Conf. Ser.* **111** (2008) 012021.
42. S. Cohen and D. Kurath, *Nucl. Phys.* **73** (1965) 1.
43. T. Dytrych *et al.*, LSU3shell: *Ab initio* no-core shell model in SU(3)-scheme basis http://sourceforge.net/projects/lsu3shell.
44. S. A. Coon, M. I. Avetian, M. K. G. Kruse, U. van Kolck, P. Maris and J. P. Vary, *Phys. Rev. C* **86** (2012) 054002.
45. R. J. Furnstahl, G. Hagen and T. Papenbrock, *Phys. Rev. C* **86** (2012) 031301.
46. S. K. Bogner, R. J. Furnstahl, P. Maris, R. J. Perry, A. Schwenk and J. Vary, *Nucl. Phys. A* **801** (2008) 21.
47. P. Maris, J. P. Vary and A. M. Shirokov, *Phys. Rev. C* **79** (2009) 014308.
48. R. Smith *et al.*, (in preparation).
49. M. Freer, E. Casarejos, L. Achouri, C. Angulo, N. I. Ashwood, N. Curtis, P. Demaret, C. Harlin, B. Laurent, M. Milin, N. A. Orr, D. Price, R. Raabe, N. Soić and V. A. Ziman, *Phys. Rev. Lett.* **96** (2006) 042501.
50. D. Suzuki, A. Shore, W. Mittig, J. J. Kolata, D. Bazin, M. Ford, T. Ahn, D. Becchetti, S. Beceiro Novo, D. Ben Ali, B. Bucher, J. Browne, X. Fang, M. Febbraro, A. Fritsch, E. Galyaev, A. M. Howard, N. Keeley, W. G. Lynch, M. Ojaruega, A. L. Roberts and X. D. Tang, *Phys. Rev. C* **87** (2013) 054301.
51. R. B. Wiringa, V. G. J. Stoks and R. Schiavilla, *Phys. Rev. C* **51** (1995) 38.
52. S. C. Pieper, V. R. Pandharipande, R. B. Wiringa and J. Carlson, *Phys. Rev. C* **64** (2001) 014001.
53. D. J. Rowe, *Rep. Prog. Phys.* **48** (1985) 1419.
54. T. Dytrych, K. D. Sviratcheva, J. P. Draayer, C. Bahri and J. P. Vary, *J. Phys. G* **35**

(2008) 123101.